Searching for signs of jet-driven negative feedback in the nearby radio galaxy UGC 05771

Henry R. M. Zovaro [1]* Nicole P. H. Nesvadba,[2] Robert Sharp,[1]
Geoffrey V. Bicknell [1] Brent Groves,[1] Dipanjan Mukherjee [3]
and Alexander Y. Wagner[4]

[1]*Research School of Astronomy and Astrophysics, The Australian National University, Canberra, ACT 2611, Australia*
[2]*Institut d'Astrophysique Spatiale, UMR 8617, Université Paris-Sud, Bât. 121, F-91405 Orsay, France*
[3]*Dipartimento di Fisica Generale, Universita degli Studi di Torino, Via Pietro Giuria 1, I-10125 Torino, Italy*
[4]*Center for Computational Sciences, University of Tsukuba, Tennodai 1-1-1, 305-0006 Tsukuba, Ibaraki, Japan*

ABSTRACT

Hydrodynamical simulations predict that the jets of young radio sources can inhibit star formation in their host galaxies by injecting heat and turbulence into the interstellar medium (ISM). To investigate jet–ISM interactions in a galaxy with a young radio source, we have carried out a multiwavelength study of the $z = 0.025$ Compact Steep Spectrum radio source hosted by the early-type galaxy UGC 05771. Using Keck/OSIRIS observations, we detected H_2 1–0 S(1) and [Fe II] emission at radii of 100s of parsecs, which traces shocked molecular and ionized gas being accelerated outwards by the jets to low velocities, creating a 'stalling wind'. At kpc radii, we detected shocked ionized gas using observations from the CALIFA survey, covering an area much larger than the pc-scale radio source. We found that existing interferometric radio observations fail to recover a large fraction of the source's total flux, indicating the likely existence of jet plasma on kpc scales, which is consistent with the extent of shocked gas in the host galaxy. To investigate the star formation efficiency in UGC 05771, we obtained IRAM CO observations to analyse the molecular gas properties. We found that UGC 05771 sits below the Kennicutt–Schmidt relation, although we were unable to definitively conclude if direct interactions from the jets are inhibiting star formation. This result shows that jets may be important in regulating star formation in the host galaxies of compact radio sources.

Key words: ISM: jets and outflows – galaxies: active – galaxies: evolution – galaxies: jets.

1 INTRODUCTION

Feedback processes driven by active galactic nuclei (AGNs) are now known to be pivotal in shaping the properties of galaxies in the modern Universe. For example, powerful quasar winds have been invoked to explain the observed galaxy luminosity function (Croton et al. 2006) and to establish correlations between properties of the stellar bulge and the mass of the central black hole (Silk & Rees 1998). Powerful, relativistic jets from radio galaxies in clusters have long been thought to prevent catastrophic cooling of the intracluster medium, reproducing observed star formation rates (SFRs; Fabian 2012; McNamara & Nulsen 2012). In recent decades, numerous observational and theoretical studies have also shown that jets can both enhance ('positive feedback') and inhibit ('negative feedback')

star formation in their host galaxies, carrying implications for the importance of radio activity in the context of galaxy evolution.

Hydrodynamical simulations suggest that jets have the potential to regulate star formation in the host galaxy, either by removing gas from the host galaxy altogether, or by heating it and thus preventing it from forming stars. When nascent jets emerge from the nucleus and propagate into the inhomogeneous interstellar medium (ISM) of their host galaxy, the jets become deflected and split as they encounter dense clumps, injecting their energy isotropically and forming a bubble that drives a shock into the ISM (Sutherland & Bicknell 2007; Wagner et al. 2016). While powerful jets may be able to expel gas from the host galaxy entirely, less powerful jets can create a 'galactic fountain', in which gas falls back towards the nucleus after being accelerated outward (Mukherjee et al. 2016), inducing turbulence into the ISM. Jets that are unable to drill efficiently through the ISM may also become temporarily trapped, injecting energy into the ISM over long periods of time.

* E-mail: henry.zovaro@anu.edu.au

Jet-induced negative feedback has now been observed in a number of radio galaxies. Many radio galaxies exhibit powerful outflows in the ionized, atomic, and molecular phases (e.g. Nesvadba et al. 2006, 2010; Morganti et al. 2013; Tadhunter et al. 2014). Warm molecular gas, traced by ro-vibrational lines of H_2, is also found in about 20–30 per cent of all massive radio galaxies, where jet-induced shocks are the most likely heating mechanism (Ogle et al. 2010; Willett et al. 2010; O'Dea 2016). The fact that ro-vibrational H_2 emission is so common in these galaxies, which are generally neither gas rich nor very actively star forming (e.g. Ocaña Flaquer et al. 2010), has previously been interpreted as evidence that jets are able to continuously inject energy into the ISM over long periods of time (e.g. Nesvadba et al. 2010). Although some of these H_2-luminous radio galaxies exhibit moderate rates of star formation, others have very low SFRs despite having large reservoirs of molecular gas (Nesvadba et al. 2010, 2011; Guillard et al. 2015), indicating that the jets are inducing negative feedback in their host galaxies.

Gigahertz peak spectrum (GPS) and Compact steep spectrum (CSS) sources are key in studying jet-induced feedback taking place within the host galaxy. They are compact ($\lesssim$20 kpc) radio galaxies characterized by a convex radio spectrum, peaking at GHz frequencies in GPS sources and at frequencies of a few 100 MHz in CSS sources, with both exhibiting a steep power-law spectrum to either side of the peak (O'Dea 1998). A larger fraction of GPS and CSS sources are asymmetric than more extended radio sources (Orienti 2016), suggesting that the jets are interacting strongly with an inhomogeneous ISM. They are also believed to represent AGNs with young jets; age estimates based on the expansion rate of the radio lobes (e.g. Giroletti et al. 2003; de Vries et al. 2009) and based on the curvature of the radio spectrum at high frequencies (Murgia 2003) are typically within the range 10^2–10^5 yr. Simulations show that jets couple most strongly to the ISM during the earliest phases of jet evolution, when the jet plasma is still confined to the host galaxy's ISM (Sutherland & Bicknell 2007; Mukherjee et al. 2016; Wagner et al. 2016). Observations of GPS and CSS sources have confirmed the ability of compact jets to kinematically disrupt the ISM, leaving signatures such as line ratios consistent with shocks, broad-line widths, and outflows of a few 1000 km s^{-1} in some sources (Holt, Tadhunter & Morganti 2008). Therefore, GPS and CSS sources are the ideal targets for observing jet-driven feedback processes which may have a significant impact upon the host galaxy's evolution.

A recent study by Zovaro et al. (2019) of the nearby CSS source 4C 31.04 demonstrated that compact jets have the potential to affect feedback processes far beyond the apparent extent of the radio source. The authors found evidence of low surface brightness jet plasma driving shocks and turbulence into the gas of the host galaxy on kpc scales, while the apparent extent of the radio jets is < 100 pc.

To establish whether the phenomenon of low surface brightness radio plasma is common in compact radio sources, and whether it plays an important role in jet-driven feedback, we build upon the work of Zovaro et al. (2019) by studying the radio source associated with the galaxy UGC 05771. It is a CSS source with a spectral peak at 150 MHz, believed to be approximately 9 pc in size (de Vries et al. 2009), and therefore a very young radio source. To search for shock-heated ionized and molecular gas within a few 100 pc of the nucleus, both important tracers of jet–ISM interactions, we obtained high-resolution, adaptive-optics-assisted near-infrared (near-IR) integral field spectrograph observations using OSIRIS on the Keck I telescope. We complemented these data with optical integral field spectroscopy from the CALIFA survey, which has a

Table 1. Properties of UGC 05771.

Property	Value	Reference
z	0.02469 ± 0.00017	Falco et al. (1999)
D_L	95.6524 Mpc	Saulder et al. (2016)
D_A	91.5876 Mpc	Saulder et al. (2016)
Angular scale	0.444 kpc arcsec^{-1}	Saulder et al. (2016)
$\log[M_*/M_\odot]$	11.27 ± 0.10	Sánchez et al. (2016)
σ_*	226 ± 3 km s^{-1}	Oh et al. (2011)
σ_e	223 ± 3 km s^{-1}	This work[a]
$\log[M_{BH}/M_\odot]$	$8.54^{+0.23}_{-0.03}$	This work[b]
n	1.25	This work[c]
R_e	3.0 kpc	This work[c]

[a]luminosity-weighted stellar velocity dispersion within the effective radius.
[b]using the M_{BH}–σ_* relation of Gültekin et al. (2009).
[c]from a Sérsic profile fit to the *V*-band continuum.

much larger field of view, enabling us to search for signatures of jet–ISM interaction on kpc scales using the optical emission line gas. To determine if the jets are inducing negative feedback in UGC 05771, we also obtained CO data from the IRAM 30 m telescope, allowing us to investigate the star formation efficiency of the host galaxy.

In Section 2, we summarize the properties of UGC 05771 and its radio source. In Section 3 we discuss our OSIRIS observations, data reduction, and analysis; in Section 4 we discuss the CALIFA data and our analysis; and in Section 5 we discuss our IRAM observations, data reduction, and analysis. We present our interpretation of our findings in Section 6 before summarizing in Section 7. For the remainder of this paper, we assume a cosmology with $H_0 = 70$ km s^{-1} Mpc^{-1}, $\Omega_M = 0.3$, and $\Omega_\Lambda = 0.7$, and use the fundamental plane-derived angular diameter distance and luminosity distance estimates of Saulder et al. (2016; Table 1).

2 HOST GALAXY AND RADIO SOURCE PROPERTIES

UGC 05771 is an early-type galaxy (ETG) with stellar mass $M_* = 10^{11.27 \pm 0.10}$ M$_\odot$, and is the most massive galaxy in a three-member group, with the stellar mass of the other two galaxies $\sim 10^{10}$ M$_\odot$ (Saulder et al. 2016). We summarize its properties in Table 1.

UGC 05771 hosts a low-power CSS source with $P_{5.0\,GHz} = 10^{22.96}$ W Hz^{-1} (Snellen et al. 2004). Fig. 1 shows the radio spectrum obtained from the integrated fluxes from the 6C 151 MHz, Texas 365 MHz, Bologna 408 MHz, Greenbank 1.4 GHz, NVSS, Becker and White 4.85 GHz, and 87GB catalogues. We also show integrated fluxes given by Snellen et al. (2004) from Jansky Very Large Array (VLA) (in BC configuration), Effelsberg observations and integrated fluxes provided by de Vries et al. (2009) using European Very Long Baseline Interferometry (VLBI) Network (EVN) and Global VLBI observations, and Very Long Baseline Array (VLBA) observations provided by Cheng & An (2018). These interferometric observations recover only $\sim$20$-$30 per cent of the flux measured using single-dish observations at similar frequencies; excluding the EVN and EVN/VLBI fluxes, the spectrum is well described by a power law at high frequencies with a spectral index $\alpha = 0.62$[1] (Snellen et al. 2004). The spectrum flattens and turns over at approximately 150 MHz.

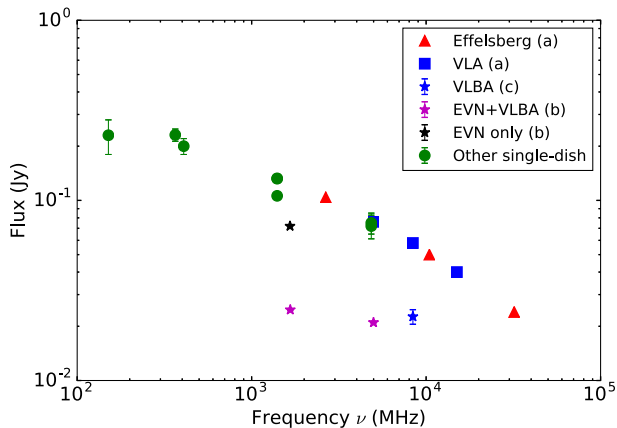[1]We define the spectral index α such that $S \propto \nu^{-\alpha}$.

Figure 1. Radio spectrum of UGC 05771. References: (a) Snellen et al. (2004); (b) de Vries et al. (2009); other single-dish fluxes are the integrated fluxes from the 6C 151 MHz, Texas 365 MHz, Bologna 408 MHz, Greenbank 1.4 GHz, NVSS, Becker and White 4.85 GHz, and 87GB catalogues.

To constrain the jet power we used the empirical correlation between radio luminosity $L_{151\,\mathrm{MHz}}$ at 151 MHz and jet power L_{jet} of Ineson et al. (2017):

$$L_{\mathrm{jet}} = 5 \times 10^{39} \left(\frac{L_{151\,\mathrm{MHz}}}{10^{28}\,\mathrm{W\,Hz^{-1}\,Sr^{-1}}} \right)^{0.89 \pm 0.09} \mathrm{erg\,s^{-1}}. \quad (1)$$

Although the correlation between jet power and radio luminosity is believed to be fairly tight for extended radio sources, Ineson et al. (2017) warn that the correlation may not hold for compact radio sources, in which the radio luminosity is expected to increase over time due to the accumulation of radiative plasma. With this caveat in mind, using the 151 MHz flux $F_{151\,\mathrm{MHz}} = 0.230$ Jy from the 6C survey, we estimate a jet power $L_{\mathrm{jet}} \geq 4.2 \times 10^{41}\,\mathrm{erg\,s^{-1}}$.

VLBI observations at 1.665 GHz (EVN and VLBA) and 4.993 GHz (EVN only), taken in 2004, reveal a symmetric core-jet structure 9 pc across with a position angle of approximately 120° (de Vries et al. 2009; Figs A1a and b). Interestingly, VLBA observations taken in 2011 at 8.4 GHz (Fig. A1c) reveal a single-sided core-jet morphology, with a bright hotspot 18.3 pc from the core to the south-east (Cheng & An 2018), and show no hints of emission along the jet axis. Although these inconsistencies are curious, they are only relevant to the parsec-scale structure of the source, which is well below the resolution limit of the observations discussed in this paper. Hence, determining the cause of these discrepancies is beyond the scope of this paper; none the less, we discuss these inconsistencies in Appendix A.

3 OSIRIS OBSERVATIONS

3.1 Observations

We observed UGC 05771 using the OH-Suppressing InfraRed Imaging Spectrograph (OSIRIS; Larkin et al. 2006) on the 10 m Keck I telescope on Mauna Kea in Hawai'i. OSIRIS is a lenslet-array integral field spectrograph operating over the wavelength range 1–2.4 μm. The instrument has a configurable plate scale (0.020, 0.035, 0.050, or 0.100 arcsec per spaxel) and a wide selection of both broad- and narrow-band filters, which determine the field of view. OSIRIS is fed by the Keck Adaptive Optics (AO) System (van Dam et al. 2006; Wizinowich et al. 2006), which can be used in laser

guide star (LGS) or natural guide star (NGS) mode, to provide near-diffraction limited angular resolution.

We used OSIRIS and the Keck AO system in LGS mode with a position angle of 0° on 2018 February 12 during the program Z260. We observed with the *H* and *K* narrow-band *Hn4* (1652–1737 nm), *Kn3* (2121–2229 nm), and *Kn4* (2208–2320 nm) filters in the 0.05 arcsec setting, providing fields of view of approximately 2.1 arcsec × 3.2 arcsec, 2.4 arcsec × 3.2 arcsec, and 2.1 arcsec × 3.2 arcsec, respectively. The median spectral resolutions in the *K* and *H* bands are approximately 3900 and 2800, respectively. We used 600 s exposure times for both source and sky frames, integrating on-source for a total of 40, 60, and 40 min in the *Hn4*, *Kn3*, and *Kn4* bands, respectively. The HIPPARCOS stars HIP41798, HIP55182, and HIP53735, observed before and after UGC 05771, were used as telluric and flux standards.

3.2 Data reduction

We reduced our observations using the OSIRIS DATA REDUCTION PIPELINE (ODRP),[2] a software package for IDL, as follows.

We mean combined our dark frames to create a master dark, which we subtracted from all science and sky frames. To associate each spectra on the detector with its corresponding lenslet, we ran the 'extract spectra' module, using the appropriate *rectification matrix* for the plate scale and filter, which provides the point spread function (PSF) for each lenslet as a function of wavelength. We then resampled the spectra to a linear wavelength grid, and assembled them into a data cube, before removing sky lines using the scaled sky subtraction method of Davies (2007). Next, we extracted 1D spectra of our telluric and flux standard stars and removed H I absorption features. We divided this 1D spectrum by a blackbody corresponding to the star's effective temperature, which we estimated using its spectral class, and normalized it to a value of 1 at the filter's effective wavelength. Lastly, we removed telluric absorption features from our object exposures by dividing the data cubes by the resulting 1D spectrum of the telluric standard.

Due to telescope pointing errors, the spatial shifts between individual exposures were not integer multiples of the spaxel size, meaning we could not use the in-built mosaicking function of the ODRP to combine our exposures. We instead created the mosaics as follows. For each data cube, we generated a continuum image by summing the data cube along the wavelength axis. We then calculated the spatial offsets for each data cube by cross-correlating the continuum images. To shift each data cube by the required amount, we used a third-order spline function to shift and interpolate each wavelength slice of the data cube. We then median combined the shifted data cubes. The associated variance of each pixel in the final data cube was calculated as the variance of the pixels contributing to the pixel value.

To flux calibrate our science exposures, we generated a 1D spectrum of the flux standard in the same fashion as for the telluric standard, and multiplied it by the normalized blackbody to restore its original spectral shape, before removing telluric absorption lines by dividing the spectrum by the 1D spectrum of the telluric standard. Then, we determined the median number of counts *n* per second in the telluric-corrected spectrum of the flux standard in a small window around the effective wavelengths of the 2MASS *Ks* band (for our *Kn3* and *Kn4* band observations) and *H* band (for our *Hn4* band observations). We created a conversion factor *T* by dividing

---

[2] Available https://github.com/Keck-DataReductionPipelines/OsirisDRP.

the expected F_λ for the flux standard, estimated using its 2MASS magnitude, by n. Lastly, we multiplied our data cubes by T to convert them from units of counts s^{-1} to $\mathrm{erg\,s}^{-1}\,\mathrm{cm}^{-2}\,\text{Å}^{-1}$.

We used a median absolute deviation (MAD) smoothing algorithm to smooth the mosaicked data cubes and to remove artefacts. For each pixel, we computed the median and standard deviation of the surrounding 8 pixels, and rejected those pixels with absolute value greater than 3 standard deviations from the median. We iterated until no more pixels were rejected. The value of the central pixel was then replaced by the mean of the remaining pixels, and the variance of the central pixel was replaced by the mean of the variance of the remaining pixels.

MAD smoothing degrades the intrinsic spatial resolution of our data σ by an amount σ_{MAD} such that the effective Gaussian sigma σ' of the PSF is increased to

$$\sigma' = \sqrt{\sigma_{\mathrm{MAD}}^2 + \sigma^2}, \tag{2}$$

where we measured σ by fitting a 2D Gaussian to our unsmoothed standard star exposures. We found the PSF of our observations to be slightly asymmetric, with $\sigma \approx 0.034\,\mathrm{arcsec} \times 0.057\,\mathrm{arcsec}$ in the *Kn3* and *Kn4* bands and $\sigma \approx 0.027\,\mathrm{arcsec} \times 0.041\,\mathrm{arcsec}$ in the *Hn4* band. We measured $\sigma_{\mathrm{MAD}} \approx 0.0459\,\mathrm{arcsec}$ by applying the MAD smoothing algorithm to 2D Gaussian profiles with known widths.

3.3 Emission line fitting

We used MPFIT (Markwardt 2009), a PYTHON implementation of the Levenberg–Marquardt algorithm (Moré 1978) developed by M. Rivers,[3] to simultaneously fit single-component Gaussian profiles to emission lines and a linear component to fit to the continuum, leaving the slope and the intercept as free parameters. We discard fits with $\chi^2 > 2$ and signal to noise (S/N) < 3. We have corrected our line widths for instrumental resolution by subtracting the width of the line spread function in quadrature from the width of the fitted Gaussian, where we estimated the width of the line spread function by fitting a Gaussian to sky lines close in wavelength to the relevant emission line.

To calculate integrated line fluxes, we summed the fluxes in each spaxel. Due to poor S/N in the $H_2\,1$–0 S(0) line, we measured the total flux by fitting a Gaussian to the co-added spectrum within the central 200 pc, corresponding to the area in which we detect $H_2\,1$–0 S(1).

To calculate upper limits for the fluxes of emission lines not detected using our χ^2 and S/N criteria, we used the following method. In each spaxel, we calculated the standard deviation σ of the continuum in a window centred on the emission line. We assumed the non-detected emission line in that spaxel was a Gaussian with amplitude 3σ. For the Br γ line, we used the width of the H α line measured using the CALIFA data (Section 4), and for non-detected H_2 lines, we used the width of the $H_2\,1$–0 S(1) line. To estimate an upper limit for the total emission line flux, we assumed the lines are detected in every spaxel in which we detect the $H_2\,1$–0 S(1) emission line.

3.4 Results

Fig. 2 shows the integrated spectra of our OSIRIS data cubes within 200 pc of the nucleus in the *Kn3* and *Hn4* bands. In the *Kn3* and *Kn4*

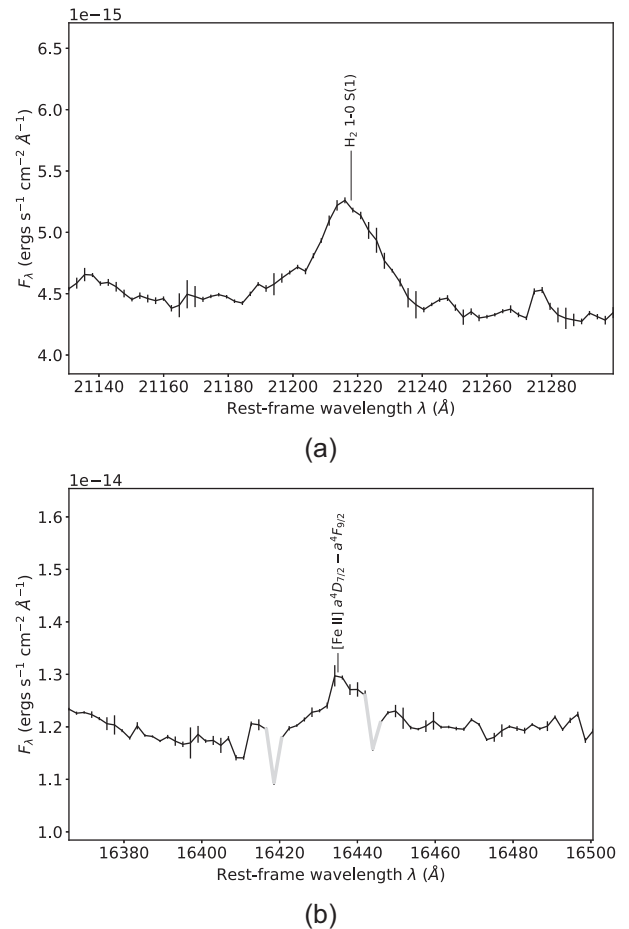[3] Available http://cars9.uchicago.edu/software/python/mpfit.html.

Figure 2. Integrated spectra extracted from the OSIRIS data cubes from spaxels within 200 pc of the nucleus in the (a) *Kn3* and (b) *Hn4* bands with 1σ error bars shown. Spectral regions dominated by sky emission have been indicated in grey.

bands, we detected ro-vibrational $H_2\,1$–0 emission lines which trace warm molecular gas, and in the *Hn4* band we detected the [Fe II] $a^4D_{7/2}$–$a^4F_{9/2}$ (rest-frame wavelength 1.644 µm) line which traces the warm ionized medium. Table 2 lists the fluxes of the detected emission lines.

3.4.1 H_2 emission

Fig. 3 shows the *Kn3* band continuum and the $H_2\,1$–0 S(1) emission line flux (rest-frame wavelength 2.122 µm), the radial velocity, and the velocity dispersion.

Ro-vibrational emission arises from several processes: hydrogen molecules can be collisionally excited by shocks, or radiatively excited by UV radiation from young stars or AGNs. The $H_2\,1$–0 S(1)/Br γ ratio can be used to distinguish between shock and UV excitation. In Fig. 4 we show the $H_2\,1$–0 S(1)/Br γ ratio in each spaxel, where we have used upper limits for the Br γ flux in each spaxel estimated using the method described in Section 3.3. The ratio far exceeds the values of 0.1–1.5 typical of regions dominated by UV excitation, strongly suggesting that the H_2 is shock heated (Puxley, Hawarden & Mountain 1990). The fact that [Fe II] emission, a tracer of shocked gas, is present in the same region (Section 3.4.2) further supports our hypothesis that the H_2 is shock heated.

Table 2. Total emission line fluxes and upper limits measured from the CALIFA data (top half of the table) and our OSIRIS observations (bottom half). For emission lines in the CALIFA and OSIRIS data, we measured the flux by simultaneously fitting Gaussian profiles to all lines in the integrated spectrum extracted from spaxels within 10 kpc and 200 pc of the nucleus, respectively. Upper limits were estimated using the method detailed in Section 3.3. Emission lines in the CALIFA data have been corrected for extinction (Section 4.3.1).

Emission line	Flux (10^{-14} erg s^{-1} cm^{-2})
[O II]$\lambda\lambda$3726,3729	7.56 ± 0.12
H β	2.18 ± 0.05
[O III]$\lambda\lambda$4959,5007	4.35 ± 0.05
[N II]$\lambda\lambda$6548,6583	7.12 ± 0.04
H α	5.64 ± 0.03
[S II]λ6716	4.10 ± 0.03
[S II]λ6731	2.25 ± 0.03
H$_2$ 1–0 S(1)	1.85 ± 0.04
H$_2$ 1–0 S(0)	0.40 ± 0.05
H$_2$ 2–1 S(1)	≤ 1
Br γ	≤ 0.3
[Fe II]	1.09 ± 0.05

In Fig. 5 we show an excitation diagram, in which the strengths of the different H$_2$ emission lines are used to estimate the relative populations of H$_2$ molecules in different rotational (J) and vibrational (v) energy levels. Using the emission line flux $I_{obs}(u, l)$ corresponding to a transition between an upper u and lower l energy level, we plot the column density of H$_2$ molecules in the upper level, $N_{obs}(v_u, J_u)$, normalized by the statistical weight g_{J_u}, from the expression of Rosenberg, van der Werf & Israel (2013):

$$\frac{N_{obs}(v_u, J_u)}{g_{J_u}} = \frac{4\pi\lambda_{u,l}}{hc} \frac{I_{obs}(u, l)}{A(u, l)}, \qquad (3)$$

where $\lambda_{u,l}$ is the rest-frame wavelength of the transition and $A_{u,l}$ is the spontaneous emission coefficient, here obtained from Wolniewicz, Simbotin & Dalgarno (1998).

We estimated the gas temperature by plotting $N(v_u, J_u)/g_{J_u}$ as a function of transition energy. In local thermodynamic equilibrium (LTE), the points will fall on a straight line in $\log N(v_u, J_u)/g_{J_u}$, where the slope of the line indicates the temperature. As we only have detections for two emission lines and an upper limit for a third, we cannot confirm whether the gas is in LTE. None the less, a linear fit to our data yields $T \approx 5000$ K.

We estimated the mass of warm H$_2$ from the flux of the H$_2$ 1–0 S(1) emission line $F_{1-0\,S(1)}$ using

$$M_{H_2}(T) = \frac{2m_p F_{1-0\,S(1)} 4\pi D_L^2}{f_{v=1, J=3}(T) A_{1-0\,S(1)} h\nu}, \qquad (4)$$

where $A_{1-0\,S(1)} = 3.47 \times 10^{-7}$ s^{-1} is the spontaneous emission coefficient (Turner, Kirby-Docken & Dalgarno 1977), $f_{v=1, J=3}(T)$ is the number fraction of H$_2$ molecules in the $v = 1$ vibrational state and $J = 3$ rotational state at temperature T, and h and c are the *Planck* constant and the speed of light, respectively. In LTE, the number fraction of molecules in a ro-vibrational state with energy E_j and degeneracy g_j is described by the Boltzmann distribution

$$f_j(T) = \frac{g_j e^{-E_j/kT}}{Z_{vr}(T)}, \qquad (5)$$

where k is the Boltzmann constant and $Z_{vr}(T) = \sum_i g_i e^{-E_i/kT}$ is the partition function, which we computed using the molecular data of Dabrowski (1984). At a temperature of 5000 K, consistent with

our excitation diagram (Fig. 5), $f_{v=1, J=3}(T) = 0.0210$. Using this value in equation (4) yields $M_{H_2}(5000\,\text{K}) = 4400 \pm 70\,\text{M}_\odot$.

3.4.2 [Fe II] emission

Fig. 6 shows the *Hn4* band continuum and the [Fe II]$_{1.644\,\mu m}$ emission line flux, the radial velocity, and the velocity dispersion.

[Fe II] emission occurs when dust grains are destroyed by fast shocks, releasing iron atoms into the ISM which are then singly ionized by the ambient radiation field. Supernovae (SNe) explosions and AGN jets or disc winds can drive shocks into the ISM, causing [Fe II] emission.

To rule out SNe explosions, we estimated the SFR required to produce the observed [Fe II] luminosity in UGC 05771, using the same approach as in Zovaro et al. (2019). First, we calculated the SNe rate $\nu_{SN, [Fe II]}$ from the [Fe II]$_{1.26\,\mu m}$ luminosity using the empirical relation for SB galaxies derived by Rosenberg, van der Werf & Israel (2012)

$$\log\left(\frac{\nu_{SN, [Fe II]}}{\text{yr}^{-1}}\right) = (1.01 \pm 0.2)\log\left(\frac{L([Fe II]_{1.26\,\mu m})}{\text{erg s}^{-1}}\right) \\ - (41.17 \pm 0.9), \qquad (6)$$

where we assumed an intrinsic ratio [Fe II] 1.26/1.64 μm =1.36, which yielded $\nu_{SN, [Fe II]} = 0.28$ yr^{-1}.

We then estimated the SNe rate from the SFR of UGC 05771, $\nu_{SN,SFR}$ using a solar metallicity STARBURST99 (Leitherer et al. 1999) model with a continuous SF law and a Salpeter initial mass function (IMF), where we estimated the SNe rate by scaling the SFR of the model to match the estimated H α-based SFR (Section 4.3.3). For ages > 1 Gyr, consistent with the stellar age of the galaxy ($\sim$10 Gyr; Sánchez et al. 2016), this gives $\nu_{SN, SFR} \approx 0.01$ yr^{-1}, an order of magnitude too small to cause the [Fe II] emission. Therefore, we conclude that SNe explosions are not the primary cause of the [Fe II] emission.

4 CALIFA OBSERVATIONS

4.1 Observations and data reduction using PIPE3D

UGC 05771 was observed using the Potsdam Multi-Aperture Spectrograph (PMAS) instrument (Roth et al. 2005) on the 3.5 m telescope at the Calar Alto observatory as a part of the Calar Alto Legacy Integral Field Area (CALIFA) survey of $0.005 < z < 0.03$ galaxies (Sánchez et al. 2012; Walcher et al. 2014; Sánchez et al. 2016). PMAS is a fibre-bundle spectrograph that produces a hexagonal data cube with 2.5 arcsec spatial resolution (FWHM) over a 74 arcsec × 64 arcsec field of view. Each galaxy in the survey was observed in both high ($R \sim 1650$) and low spectral resolution ($R \sim 850$) modes of PMAS, covering wavelength ranges of 3700–4800 Å and 3749–7500 Å, respectively. The spectral resolution of the high- and low-resolution modes corresponds to velocity dispersions of approximately 100 km s^{-1} < σ < 200 km s^{-1} and 60 km s^{-1} < σ < 80 km s^{-1}, respectively. We show the spectrum extracted from the 'combined' data cube, which merges the high- and low-resolution spectra into a single data cube, from spaxels within 5 kpc of the nucleus in Fig. 7.

We used the data products produced by PIPE3D, a processing pipeline developed for integral field unit surveys (Sánchez et al. 2016) developed by the CALIFA collaboration, to study the spatially resolved stellar population and ionized gas properties of UGC 05771. To elevate the S/N to a level sufficient for analysis
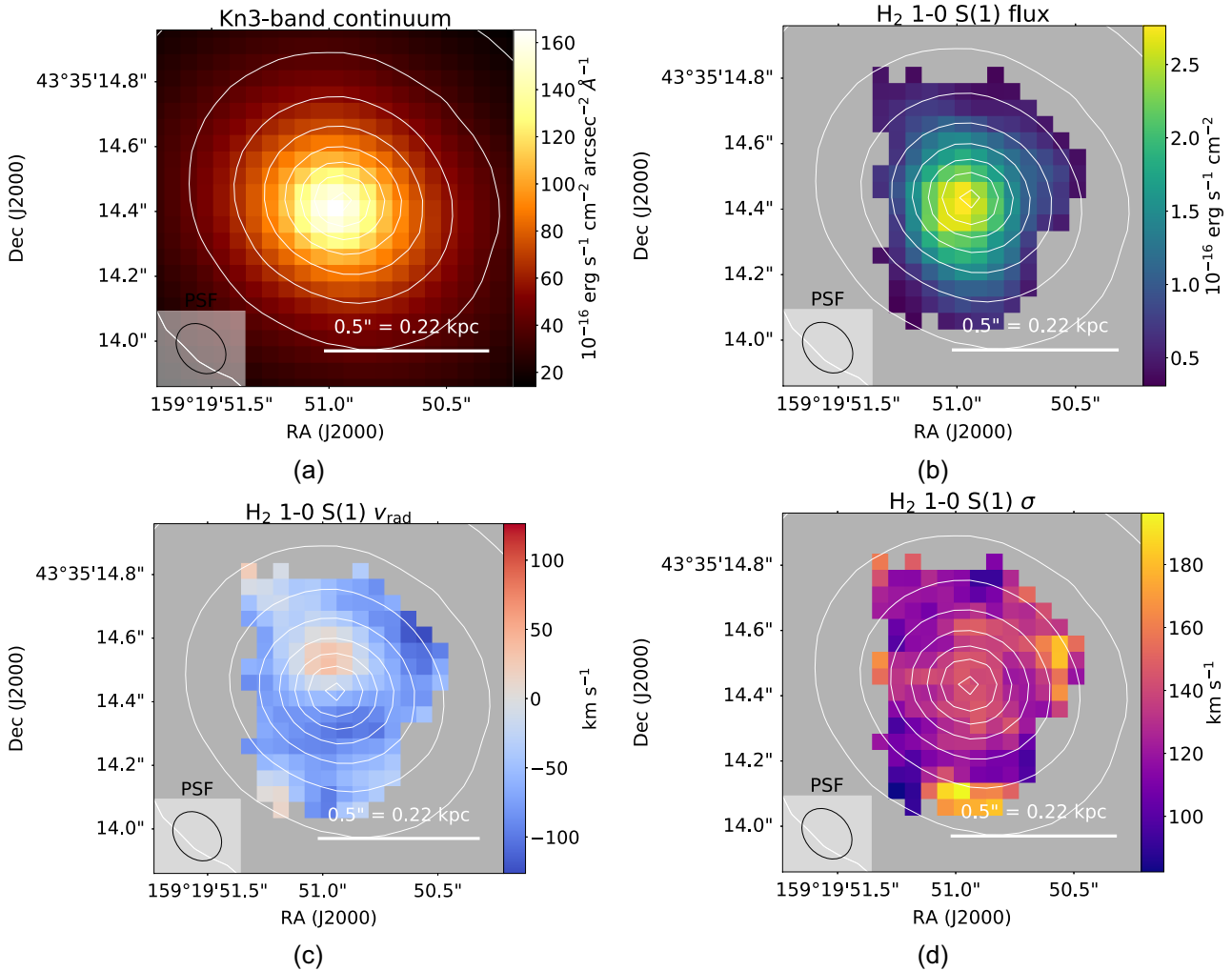
Figure 3. (a) The *Kn3* band continuum, (b) the integrated flux, (c) radial velocity (relative to rest-frame wavelength), and (d) velocity dispersion of the H_2 1–0 S(1) emission line. The *Kn3* band continuum is indicated in contours, and the full width at half-maximum (FWHM) of the PSF (taking into account the effects of MAD smoothing) is indicated in all figures.
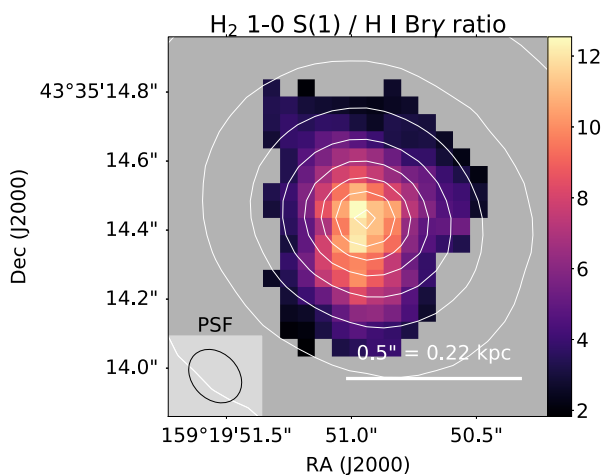

Figure 4. A map showing the H_2 1–0 S(1)/Br γ ratio in each spaxel. The large values of this ratio suggest shocks are the excitation mechanism. The *Kn3* band continuum is indicated in contours, and the FWHM of the PSF (taking into account the effects of MAD smoothing) is indicated.
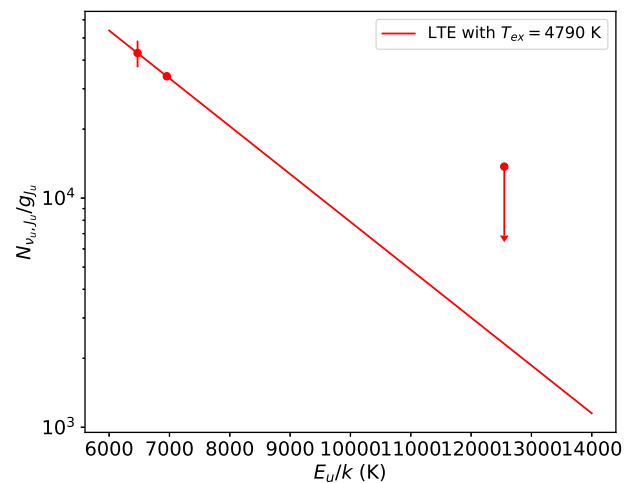
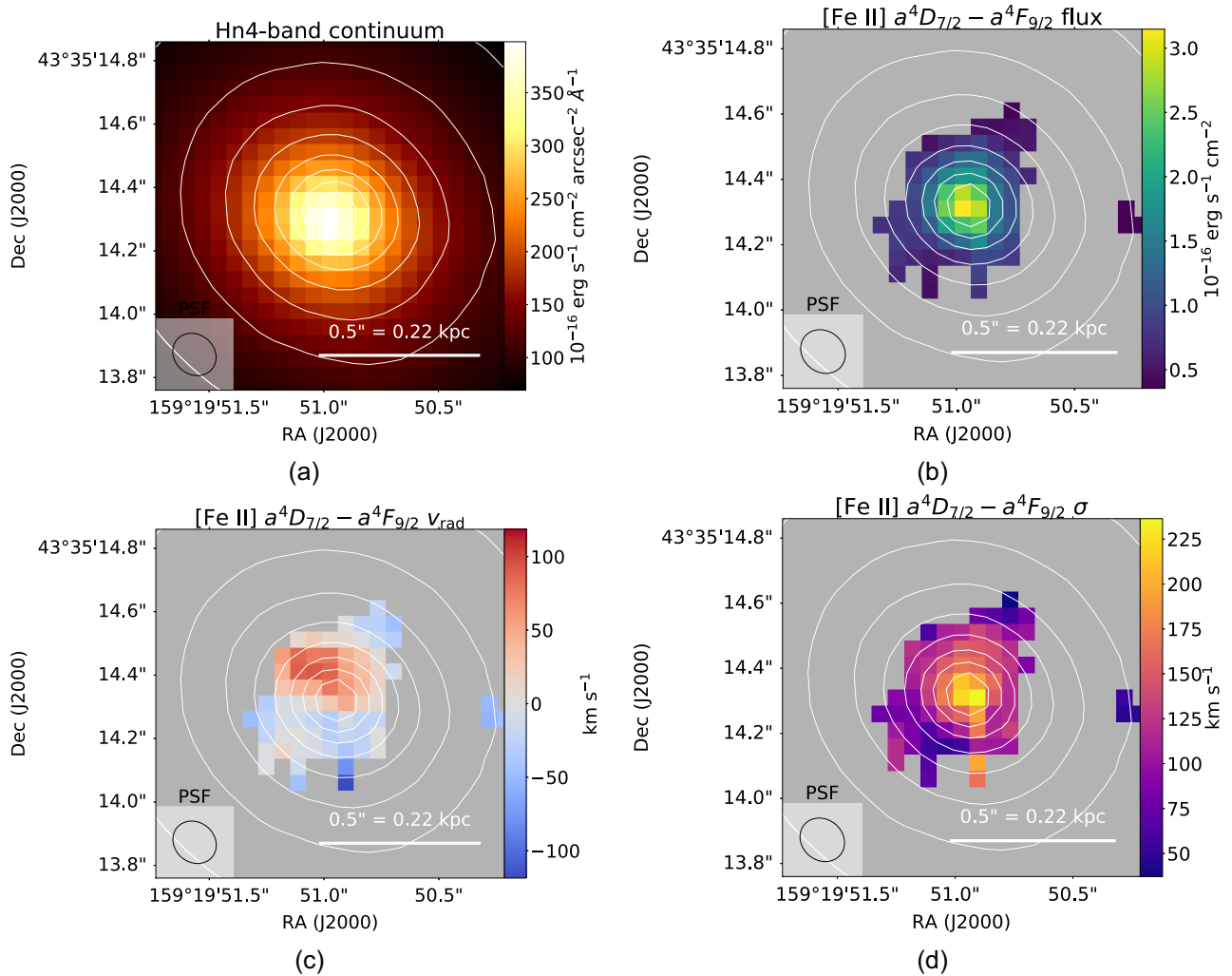**Figure 5.** Excitation diagram, where we indicate the line of best fit.

Figure 6. (a) The *Hn4* band continuum, (b) the integrated flux, (c) radial velocity (relative to rest-frame wavelength), and (d) velocity dispersion of the [Fe II] emission line. The *Hn4* band continuum is indicated in contours, and the FWHM of the PSF (taking into account the effects of MAD smoothing) is indicated in all figures.
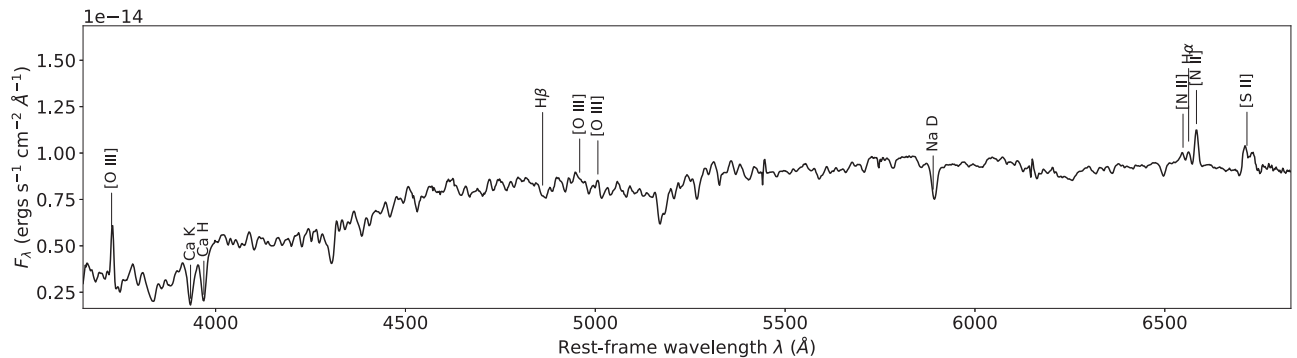

Figure 7. Integrated spectrum extracted from the CALIFA data cube from spaxels within 5 kpc of the nucleus.

of the stellar continuum, PIPE3D spatially bins the data cube, before fitting spectral templates to the spectra to provide quantities including the kinematics, metallicity, and ages of the stellar population. The stellar continuum fit to each spaxel is then subtracted from the data cube, yielding an emission line-only data cube, to enable analysis of the emission line spectra.

4.2 Stellar properties

The best-fitting stellar population of UGC 05771 produced by PIPE3D is predominantly old, with a star formation history well approximated by an instantaneous burst ∼10 Gyr ago. Fig. 8 shows the *V*-band continuum reconstructed using the data cube, the stellar radial velocity, and the velocity dispersion.
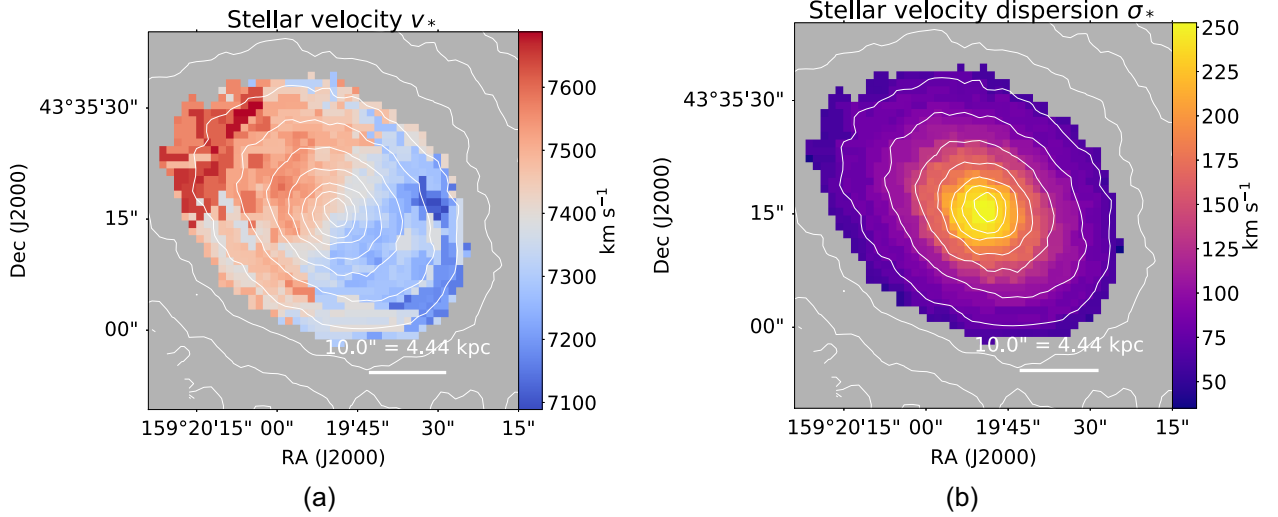
Figure 8. (a) The stellar radial velocity, relative to systemic, and (b) velocity dispersion (Gaussian σ). The contours indicate the logarithmically scaled *V*-band continuum.

We estimated the black hole mass using the $M_{\rm BH}$–σ_* relation of Gültekin et al. (2009) given by

$$\log_{10}\left[\frac{M_{\rm BH}}{\rm M_\odot}\right] = (8.23 \pm 0.08) \pm (3.96 \pm 0.42)$$
$$\times \log_{10}\left[\frac{\sigma_{\rm e}}{200\,{\rm km\,s^{-1}}}\right], \qquad (7)$$

where $\sigma_{\rm e}$ is the luminosity-weighted stellar velocity dispersion within the effective radius $R_{\rm e}$. We calculated $\sigma_{\rm e}$ from the average flux intensity I_i and stellar velocity dispersion $\sigma_{*,i}$ in each spaxel i using

$$\sigma_{\rm e} = \frac{\sum_i I_i \sigma_{*,i}}{\sum_i \sigma_{*,i}}. \qquad (8)$$

We calculated $\sigma_{\rm e}$ within 1 $R_{\rm e}$, which we estimated by fitting a Sérsic profile to the *V*-band continuum image constructed from the data cube, which yields $\sigma_{*,i} = 226 \pm 3\,{\rm km\,s^{-1}}$. Using this value, we estimated $\log_{10} M_{\rm BH} = 8.54 \pm^{0.23}_{0.03} \log {\rm M_\odot}$.

4.3 Emission line analysis

We performed our own Gaussian emission line fits to the emission line-only data cube using the method detailed in Section 3.3. We simultaneously fitted the emission lines [O II]$\lambda\lambda$3726,3729, H β, [O III]$\lambda\lambda$4959,5007, [N II]$\lambda\lambda$6548,6583, H α, [S II]λ6716, and [S II]λ6731, where we constrained each line to have the same kinematics, and we fixed the relative fluxes of the lines in the [N II] and [O III] doublets to their expected values of 1:3.06 and 1:2.94, respectively. Due to the low spectral resolution of PMAS at the wavelengths of most emission lines, we only fitted a single kinematic component to each line.

We show the total extinction-corrected emission line fluxes in Table 2, where we have summed fluxes from spaxels with fits that have S/N > 3 and reduced χ^2 < 2. The ionized gas kinematics are shown in Fig. 9, where we present the H α flux, the radial velocity, and the velocity dispersion.

4.3.1 Reddening

To correct our emission line fluxes for extinction, we used the reddening curve of Fitzpatrick & Massa (2007) with $R_V = 3.1$, assuming that the ratio of the intrinsic line fluxes $I({\rm H}\alpha)/I({\rm H}\beta) = 2.85$ corresponding to Case B recombination. We calculated the total extinction in the *V* band, A_V, in each spaxel in which the line ratio had a S/N > 3 (Fig. 10). There were a number of spaxels in which the ratio of the observed fluxes $\frac{F({\rm H}\alpha)}{F({\rm H}\beta)} < 2.85$, corresponding to values of $A_V < 0$; these non-physical line ratios are most likely due to systematic errors in fitting the underlying stellar continuum.

To estimate the mean A_V, we calculated the average of the H α/H β ratios in each spaxel in which the ratio has S/N > 3 and $\frac{F({\rm H}\alpha)}{F({\rm H}\beta)} > 2.85$, which yielded $A_V = 0.831 \pm 0.014$.

In spaxels where the H β S/N < 3 but H α is still detected, we estimated upper limits for the H β flux using the method detailed in Section 3.3, which provided a lower limit for A_V. In spaxels closer to the nucleus, $A_V \gtrsim 0.5$, at larger radii, where the H α surface brightness drops off, we cannot provide any meaningful constraint on A_V. Therefore, without any further information, we assumed $A_V = 0.831 \pm 0.014$ across the whole galaxy, and have used this value to correct for extinction in the line fluxes given in Table 2.

We also used A_V to estimate the hydrogen column density $N_{\rm H}$ using the relation of Güver & Özel (2009). In the spaxels over which we could measure A_V, the mean column density $N_{\rm H} = 1.84 \pm 0.03 \times 10^{21}\,{\rm cm^{-2}}$. We estimated the total hydrogen mass from the column densities in each spaxel i using $M_{\rm H} = \sum_i \mu m_{\rm H} N_{\rm H,i} A_i \geq 4.7 \pm 0.2 \times 10^8\,{\rm M_\odot}$ where $\mu = 1.37$ is the mean molecular mass, $m_{\rm H}$ is the mass of the hydrogen atom, and A_i is the area of each spaxel in ${\rm cm^2}$. This gave a mean molecular gas mass surface density $\Sigma_{\rm gas} = 10.0 \pm 0.5\,{\rm M_\odot\,pc^{-2}}$ which is consistent with our estimate based on our CO observations ($\Sigma_{\rm gas} = 15 \pm 5\,{\rm M_\odot\,pc^{-2}}$; Section 5).

4.3.2 Excitation mechanism

To investigate the excitation source of the ionized gas, we constructed optical diagnostic diagrams (ODDs; Baldwin, Phillips & Terlevich 1981; Veilleux & Osterbrock 1987; Kewley et al. 2001;
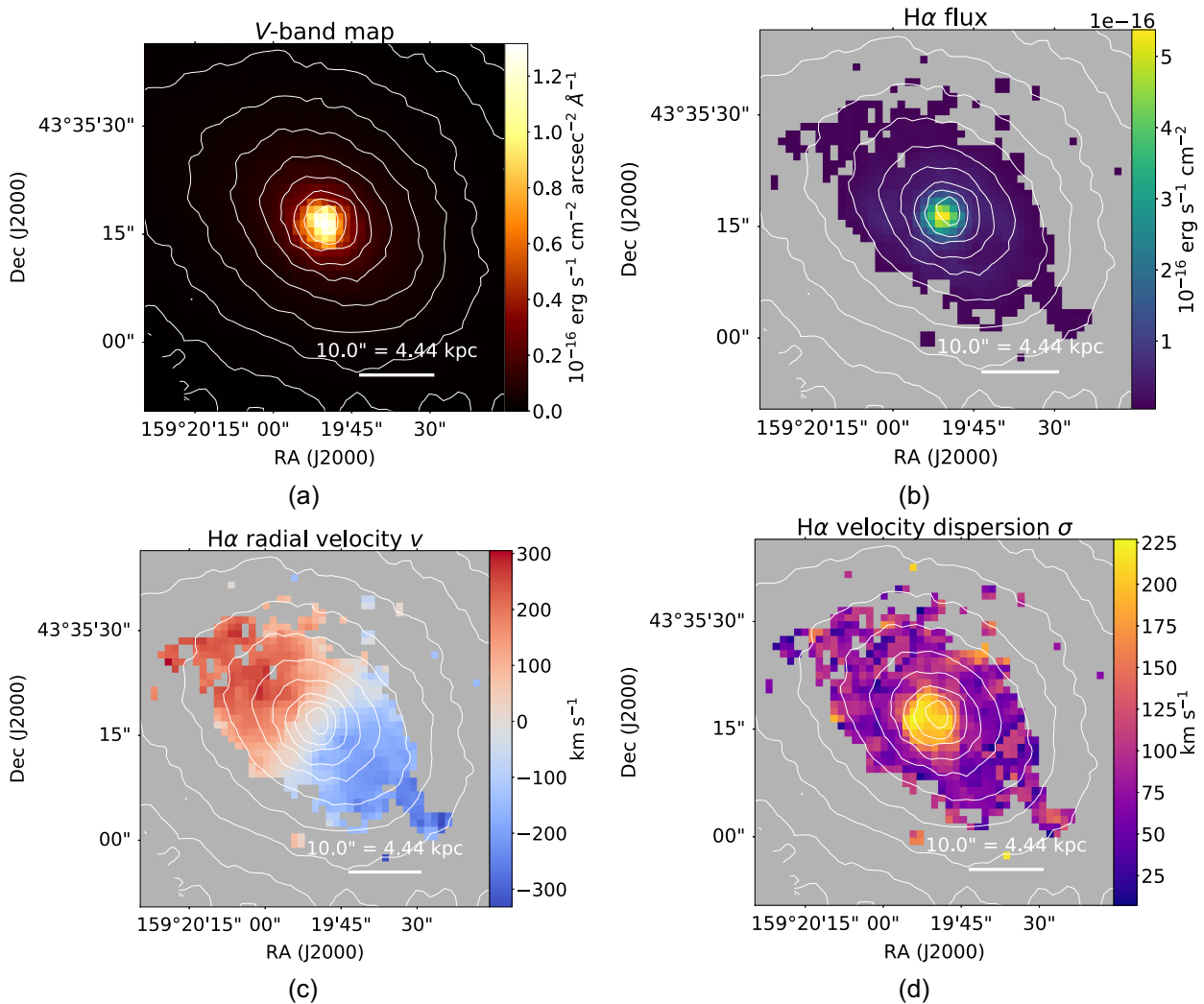
Figure 9. (a) *V*-band continuum; (b) H α emission line flux, (c) radial velocity (relative to systemic), and (d) velocity dispersion (Gaussian σ), corrected for the instrumental dispersion. Contours show the logarithmically scaled *V*-band continuum.
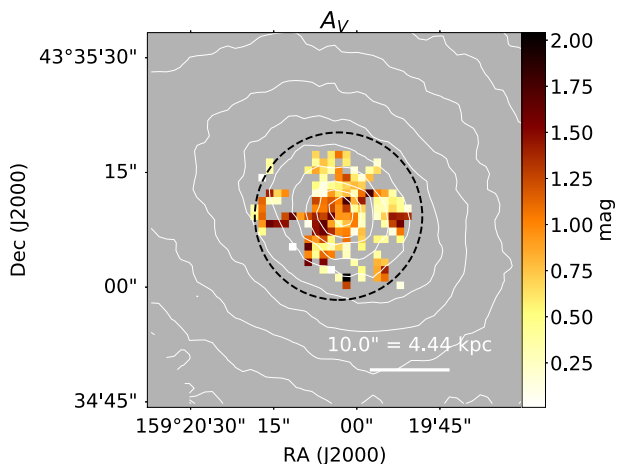

Figure 10. Total extinction in the *V*-band A_V. The contours indicate the logarithmically scaled *V*-band continuum, and the dashed circle shows the FWHM of the IRAM 30 m telescope beam at the observed frequency of the CO(1–0) line (Section 5).

Kauffmann et al. 2003; Kewley et al. 2006). In an ODD, the ratios of certain pairs of emission line fluxes are plotted against one another to distinguish between excitation due to shocks, photoionization from stellar radiation fields, and harder radiation fields from AGNs.

In Fig. 11(a), we show the spaxel-by-spaxel ODDs for UGC 05771, where each spaxel is colour coded by its projected distance from the nucleus in the plane of the sky. We used the line fluxes and velocity dispersion from our Gaussian fit, only including spaxels in which the S/N of all lines exceeds 3, except for the [O I]λ6300 line for which we used the flux from the Monte Carlo-method fit provided by PIPE3D (Sánchez et al. 2016, section 3.6) because the S/N in this line was too low to be fit using our own method. In all three ODDs, most spaxels lie above the maximum [O III]/H β ratio that can arise from star formation alone at a given [N II]/H α ratio (the solid curve) of Kewley et al. (2001).

Despite their diagnostic power, line ratios alone cannot be used to distinguish between photoionization and shock excitation for spaxels with low-ionization nuclear emission line region (LINER)-like emission, which otherwise occupy overlapping regions to the right of all three ODDs. For this reason, in Fig. 11(b) we show
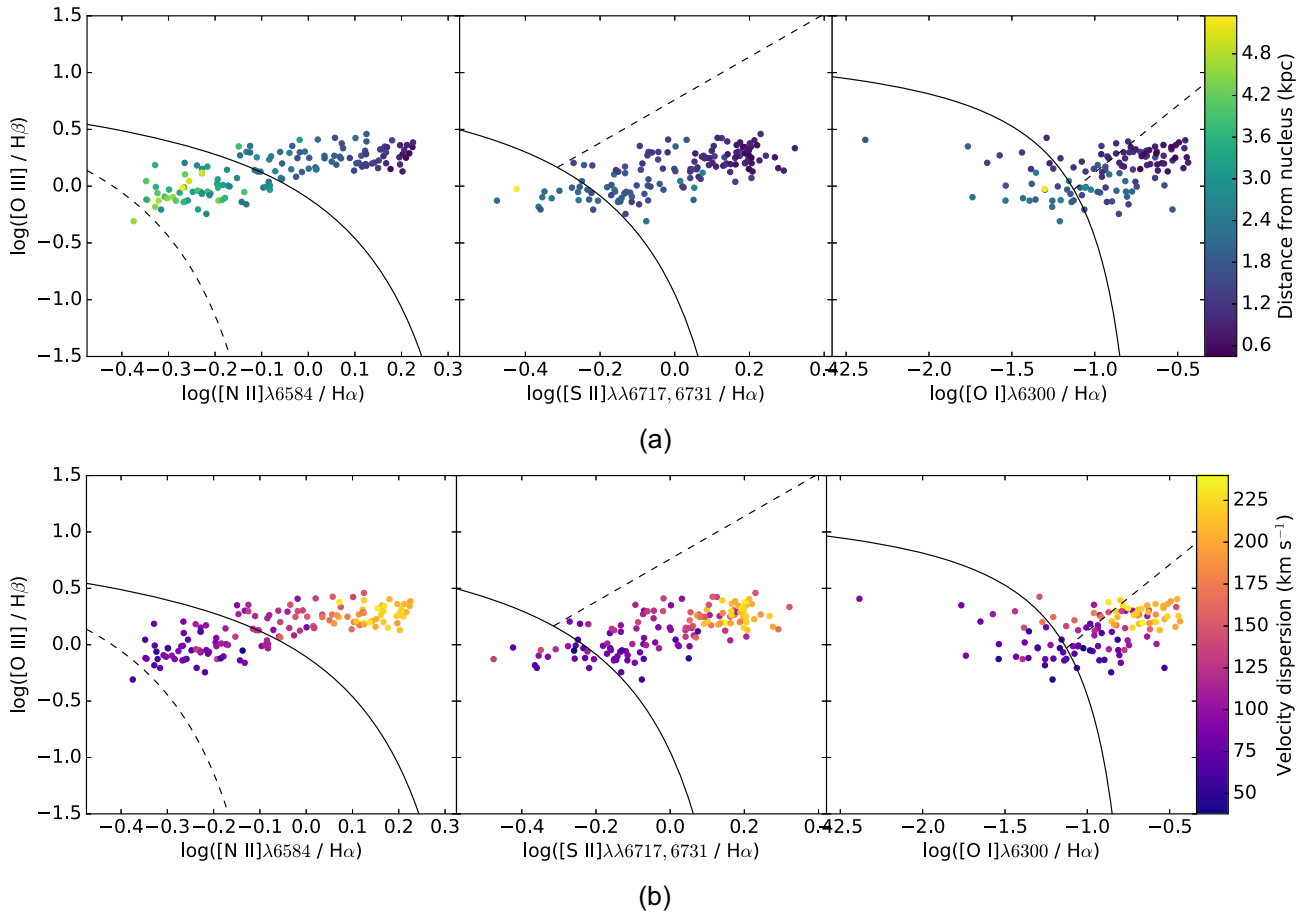
Figure 11. Optical diagnostic diagrams for spaxels in UGC 05771 (Baldwin et al. 1981; Veilleux & Osterbrock 1987) with points coloured by (a) their distance from the nucleus (assumed to coincide with the peak in the *V*-band continuum) and (b) by the H α velocity dispersion. The solid lines represent the maximum [O III]/H β ratio that can arise from star formation alone, derived from photoionization models (Kewley et al. 2001). In the left-hand panels, the dashed line is the equivalent empirical relation of Kauffmann et al. (2003) which separates star-forming galaxies and AGN hosts. In the middle and right-hand panels, the dashed lines separate Seyfert-like (above) and LINER-like ratios (below the line) (Kewley et al. 2006).

the same ODDs with the spaxels colour coded by the H α velocity dispersion, which reveals that the spaxels with the largest [N II]/H α ratios are also those with the highest velocity dispersion, indicating shocks dominate the line emission.

Although we cannot rule out shocks as the excitation mechanism for the line emission in the outer regions of the galaxy, the lower velocity dispersion in these regions is consistent with line emission powered by a diffuse ionization field, probably from evolved stars (Singh et al. 2013; Belfiore et al. 2016). This is consistent with the ∼10 Gyr old stellar population of UGC 05771, in which post-AGB stars, hot and evolved stars that emit a hard ionizing spectrum, are expected to dominate the ionization field, contaminating SFR estimates based on the H α flux and FUV magnitude. We discuss the implications of this in the following section.

4.3.3 Star formation rate estimate

Using the total extinction-corrected H α flux and the calibration of Calzetti (2013) derived from stellar population modelling using a Kroupa IMF, we estimated the global SFR(H α) = 0.2795 ± 0.0011 $M_\odot$ yr^{-1}. However, we are confident this is an upper limit due to contamination from other sources of H α emission. Inspection of Fig. 9(b) reveals that the H α emission peaks sharply within a

few kpc of the nucleus, which is also where we observe very strong shock signatures (Fig. 11). Therefore a substantial portion of the total H α flux is due to shocks.

To obtain a more strict upper limit to the SFR, we used the ODDs presented in Section 4.3.2. Although many spaxels lie in the LINER region of the ODD, a significant number of spaxels occupy the intermediate region (between the dashed and solid curves in the left-hand panels of Figs 11a and b), in which the line ratios indicate that both star formation and shocks and/or radiation from post-AGB stars contribute to the line emission. To obtain a better upper limit for the SFR, we only included the H α flux from spaxels that lie in the intermediate and star-forming regions. Unfortunately, there are many spaxels that we could not show on the ODDs due to poor S/N in [O III] and H β. However, these spaxels are predominantly at large radii, where the surface brightness is low and inspection of Fig. 11(a) shows that there are very few spaxels at radii ≳2 kpc that lie in the LINER region. Hence, we assumed that all spaxels at large radii with unknown line ratios lie in the intermediate or star-forming regions of the ODD. Summing the H α fluxes from all spaxels in the intermediate or star-forming regions yield SFR(H α) = 0.1046 ± 0.0007 $M_\odot$ yr^{-1}. We stress that this again represents an upper limit, as the majority of these spaxels lie in the intermediate region, implying contributions from sources other than star formation.

To determine whether there is any significant star formation obscured by extinction, we also estimated the SFR using far-infrared (far-IR) fluxes from the *Infrared Astronomical Satellite* (*IRAS*; Neugebauer et al. 1984). Because UGC 05771 was not detected by *IRAS*, we instead used the *IRAS* Scan Processing and Integration tool[4] to estimate upper limits from the total integrated flux density within ±2.5 arcmin of UGC 05771. Using the 60 μm flux density upper limit of $f_\nu(60\,\mu\mathrm{m}) = 0.12$ Jy and the total IR (TIR) bolometric correction $L_{\mathrm{TIR}} = 1.7 L_{60\,\mu\mathrm{m}}$ of Rowan-Robinson et al. (1997) and the TIR SFR calibration of Kennicutt (1998), we obtained SFR(TIR) $< 0.5\,\mathrm{M_\odot\,yr^{-1}}$. Given that the FIR fluxes may also be contaminated by the AGNs, this confirms that there is unlikely to be a significant amount of obscured star formation, which is expected given the modest A_V we estimate from our H α and H β fluxes.

We also estimated the SFR using the *Galaxy Evolution Explorer* far-UV magnitude. After correcting for reddening, and using the UV SFR law of Salim et al. (2007), we found SFR(UV) $= 0.94 \pm 0.12\,\mathrm{M_\odot\,yr^{-1}}$, much larger than that based on the H α and far-IR fluxes. However, the UV flux is likely to be strongly contaminated by emission from old stars; as discussed above, LINER-like emission line ratios suggest that post-AGB stars most likely dominate the UV radiation field in the outer regions of the galaxy. Hence, SFR(UV) represents a strict upper limit.

Therefore, because SFR(TIR), SFR(UV), and SFR(H α) represent strict upper limits, we conclude that the true SFR in UGC 05771 is most likely lower than SFR(H α) $= 0.1046 \pm 0.0007\,\mathrm{M_\odot\,yr^{-1}}$. We use this latter estimate of the SFR to investigate the star formation efficiency in UGC 05771 in Section 7.

4.3.4 Ionized gas kinematics

Fig. 9 shows the H α flux, the radial velocity, and the velocity dispersion. Upon first inspection, there are no obvious signs of disrupted kinematics in the H α radial velocity. This is perhaps to be expected, given the low radio luminosity of the source, which is several orders of magnitude lower than those of the sample of GPS and CSS sources of Holt et al. (2008) in which outflows of up to a few 1000 km s^{-1} are observed.

None the less, to determine whether there are any significant non-circular motions in the ionized gas, we fitted a disc model to the radial velocity data using MPFIT. We first fitted a Sérsic profile to the galaxy's light profile along its semimajor axis in the *V*-band continuum (Fig. 9a); we show the Sérsic parameters in Table 1. We then used the analytical expressions of Terzić & Graham (2005) for the circular velocity in a Sérsic potential, which also requires the total galaxy mass; we used the mass estimated by Sánchez et al. (2016) (Table 1). We fitted the circular velocity profile to our data, allowing the systemic velocity, inclination, and position angle to vary. We constrained the kinematic centre of the disc to coincide with the peak in the *V*-band continuum.

Fig. 12 shows our model fit and residuals to the radial velocity of the H α disc. The $\chi^2 > 10$, indicating a poor fit for our rather simplistic disc model. To ensure that any disturbed kinematics in the central region were not biasing the fit, we reran our fit with the central 2 kpc masked. The best-fitting parameters were almost identical in both cases, indicating that the kinematics in the nuclear region were not significantly biasing the fit. The residual reveals a counter-rotating structure in the nucleus and a velocity gradient on larger scales in the disc. Although counter-rotating cores are not

uncommon in ETGs (e.g. Bender 1988), this may also indicate that our simple disc model is a poor fit to the data.

The H α velocity dispersion (Fig. 9d) is clearly elevated within 2 kpc of the nucleus, reaching values $\sigma \gtrsim 225$ km s^{-1}. Whilst the velocity dispersion in most parts of the disc does not exceed 100 km s^{-1}, the velocity dispersion within about 2 kpc of the nucleus reaches values as high as 225 km s^{-1}.

To determine whether the enhanced central velocity dispersion could be due to beam smearing, we used our best-fitting disc model to obtain line-of-sight (LOS) velocities, which we then used to create synthetic emission lines in each spaxel of a data cube. We modelled each emission line with an intrinsic Gaussian σ of 75 km s^{-1}, to match the observed velocity dispersion in the outer regions of the gas disc, plus the instrumental resolution of PMAS. We spatially smoothed the cube to match the 2.5 arcsec seeing of the CALIFA data, and then spatially binned the cube to match the spaxel size. Finally we added Gaussian noise to replicate the S/N in the CALIFA data. By measuring the velocity dispersion in each spaxel using our emission line fitting routine, we found that beam smearing was unable to reproduce the observed line widths in the central 2 kpc. We hence rule out beam smearing as the sole cause of the elevated velocity dispersion in this region.

An alternative scenario to explain the high velocity dispersions and shock-like line ratios in the inner parts of the disc of UGC 05771 could be accretion of gas from the surroundings of the galaxy. In principle, such an accretion event could also have triggered the nuclear activity. UGC 05771 resides in a group environment with two massive galaxies within a few 100 kpc. Hence, a recent encounter or minor merger would not be implausible, although we do not see any evidence for that, e.g. in the stellar morphology of UGC 05771. Moreover, mass accretion rates required to fuel nuclear radio activity are very low, of order $10^{-3}\,\mathrm{M_\odot\,yr^{-1}}$ or less (e.g. Merloni, Heinz & di Matteo 2003), so that a specific triggering event may not be necessary. We also do not see any signatures of infalling neutral gas, such as interstellar Na D absorption line components, and the rotation of the gas disc is overall very regular (Fig. 9c); this is inconsistent with a recent merger event that would have been strong enough to stir up large parts of the gas in the nuclear regions.

An exception might be the small region within 2 kpc of the nucleus where we find non-circular motions, which could originate from a counter-rotating core, if this feature is not due to an interaction with extended jet plasma. However, for accreted gas to become bound to the disc, it cannot have a velocity much larger than the circular velocity of the disc, which is approximately 100 km s^{-1} within the inner kpc (Fig. 12d). Basic energy conservation arguments would therefore make it unlikely that such gas can cause the observed velocity dispersions of 225 km s^{-1}, which are much greater, even when neglecting that much of the kinetic energy of the gas is being radiated away by line emission from shocked gas. We therefore do not consider accretion a strong alternative explanation, although detailed, high-resolution hydrodynamical simulations of rapid gas accretion events would be very useful to explore this alternative further.

5 IRAM OBSERVATIONS

5.1 Observations

We obtained CO(1–0) and CO(2–1) spectra of UGC 05771 with the IRAM 30 m telescope through the Institut de Radio Astronomie Millimétrique (IRAM) Director's Discretionary Program D06-18
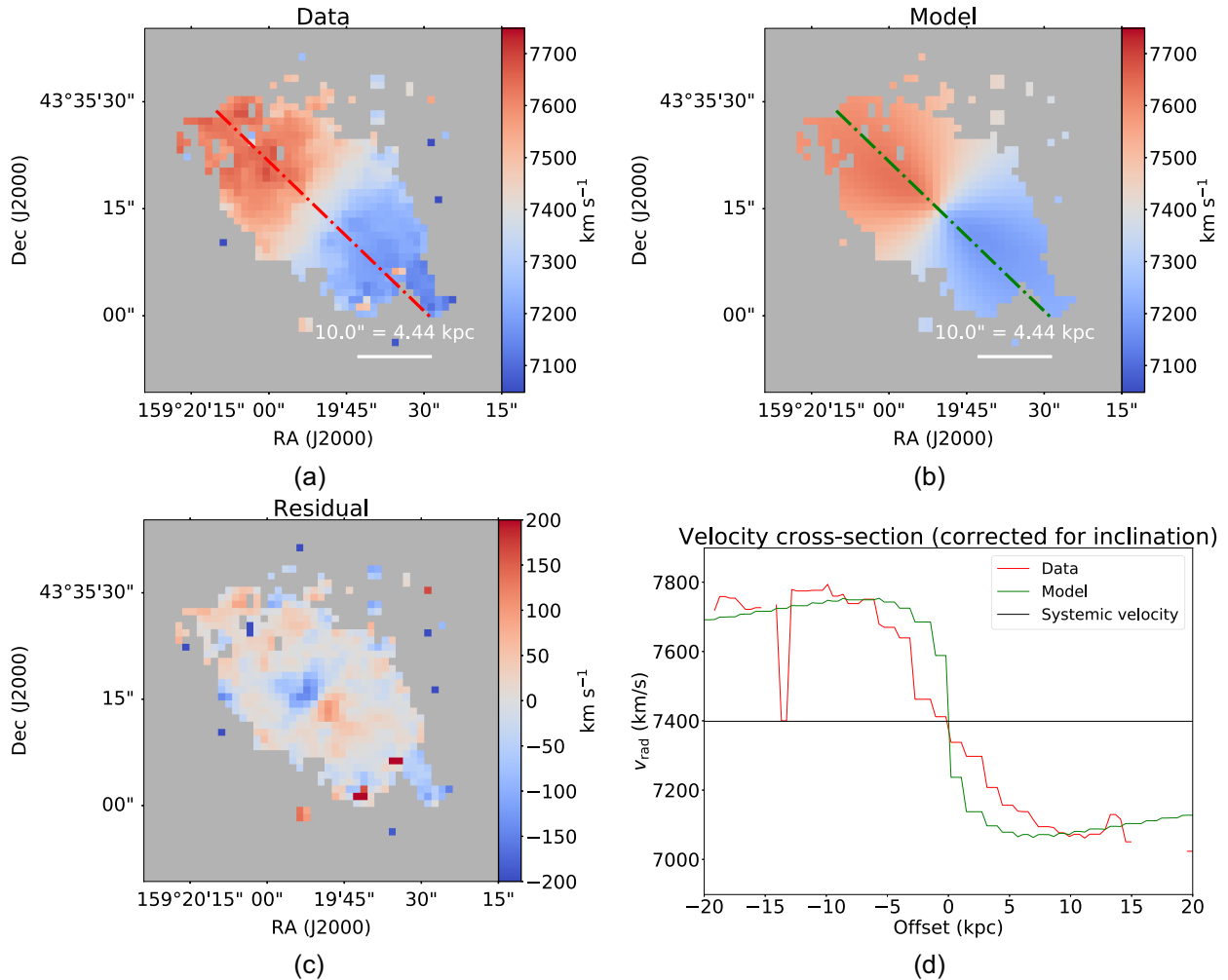
---

[4]Available https://irsa.ipac.caltech.edu/applications/Scanpi/.

Figure 12. (a) H α radial velocity from the Gaussian fit, (b) Sérsic disc model fit, (c) velocity residuals, and (d) a plot showing the radial velocity along the dashed green and red lines in panels (a) and (b), corrected for inclination. In panel (c), subtracting the model fit reveals a counter-rotating structure in the central region of the galaxy. The velocities in panels (a) and (b) are given with respect to the local standard of rest.

on 2019 February 25th. The source was observed with the Eight MIxer Receiver (EMIR), a wide-band heterodyne receiver, as part of the heterodyne pool. Both lines were observed together in dual-band mode with the FTS200 and The Wideband Line Multiple Autocorrelator (WILMA) backends. They were placed in the UI sideband, with a tuning frequency corresponding to the expected observed frequencies ν_{obs} of the lines at $z = 0.02469$, 112.494 GHz, and 224.983 GHz for CO(1–0) and CO(2–1), respectively. The IRAM beam FWHM is 21.8 arcsec at 114 GHz and 10.6 arcsec at 228 GHz.

We used Wobbler switching throws of 60 arcsec, which is larger than the size of CO line emission in UGC 05771. The telescope was focused at the beginning of the observations on the bright quasar 1226+023, and then refocused every 3–4 h. Another quasar, 0923+392, which is near the source, was used to reposition the telescope on the sky every 2–3 h. Individual scans were 30 s long, and we obtained a calibration after sequences of 12 scans, i.e. every 6 min. The precipitable water vapour during observations varied between 1.5 and 5 mm. The total time on-source was 14580 s.

5.2 Data reduction

The data were calibrated at the telescope, and reduced with the CLASS package of the IRAM GILDAS software (Gildas Team 2013).

All scans were examined by eye, and first-order polynomials were used to correct the baselines, after masking the spectral range covered by the line. We then averaged the individual scans, combining both horizontal and vertical polarizations. We used the antennas efficiencies given on the EMIR website of 5.9 Jy K^{-1} for the 3 mm, and 7.5 Jy K^{-1} for the 1.3 mm data to translate the measured brightness temperatures into flux density units, i.e. Jy. The lines are detected with both backends. We used WILMA to extract the scientific results, because it has a spectral resolution better suited to measurements of extragalactic emission lines, and more stable baselines. The resulting root-mean-square (rms) noise is 5.3 and 7.5 mJy for CO(1–0) and CO(2–1), respectively, for a spectral channel width of 5 km s^{-1} at 112.5 GHz.

5.3 Results

We show the CO(1–0) and CO(2–1) spectra of UGC 05771 in Fig. 13, and the details of our observations and the fitted Gaussian profiles in Table 3. Both lines were clearly detected at the expected redshifts.

The CO(1–0) line shows a possible double-peaked profile, with a total line width of FWHM $= 476 \pm 23$ km s^{-1}. The CO(2–1) line is somewhat broader, with FWHM $= 562 \pm 26$ km s^{-1}, and
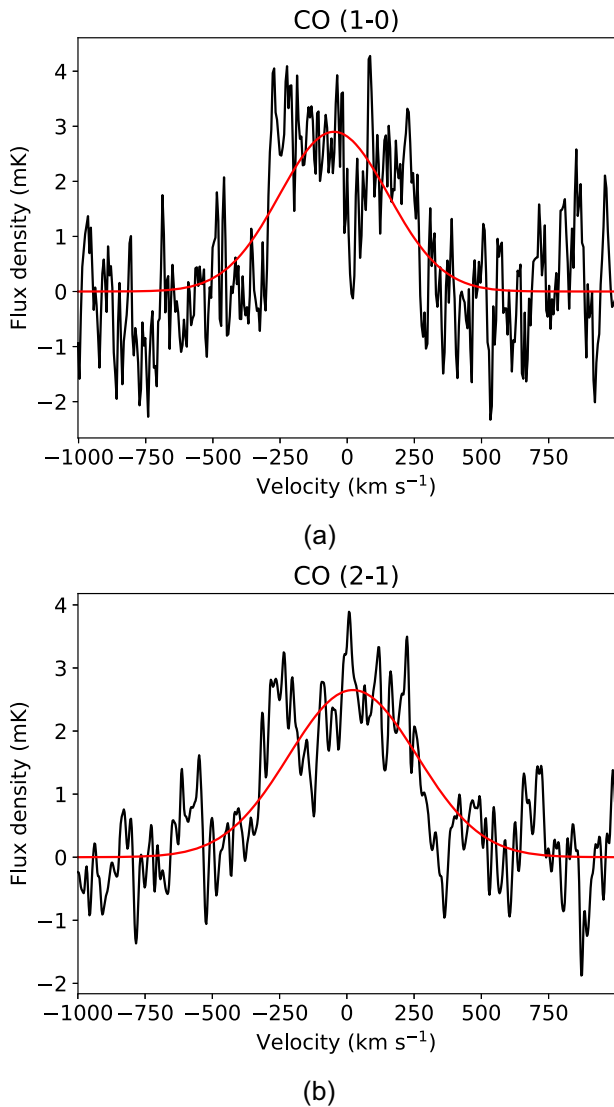
CO (1-0)

CO (2-1)

Figure 13. (a) CO(1–0) and (b) CO(2–1) line profiles of UGC 05771. Red lines show the best Gaussian fit to each line.

appears to have a more complex line profile, although this may be due to the lower S/N and more irregular baselines at 1.3 mm. The CO(1–0) and CO(2–1) lines are centred around velocities of 49 ± 13 and $22 \pm 11 \,\mathrm{km\,s^{-1}}$, respectively, relative to the systemic redshift of UGC 05771. The broad widths of the CO line profiles are consistent with the radial velocities observed in the ionized gas disc ($v_{\mathrm{rad}} \approx 200 \,\mathrm{km\,s^{-1}}$, Fig. 9c) suggesting the broad-line widths are dominated by rotation, although additional broadening due to turbulence may be present. The line fluxes are 8.6 ± 0.4 and $11.9 \pm 0.5 \,\mathrm{Jy\,km\,s^{-1}}$ for CO(1–0) and CO(2–1), respectively. The line ratio CO(2–1)/CO(1–0) = 2.5 is consistent with those in the sample of powerful radio galaxies with CO observations by Ocaña Flaquer et al. (2010), although this ratio may be affected by the different beam sizes of the 30 m telescope at 3 and 1.3 mm, which would have an effect if the CO reservoir is more extended than the 10 arcsec beam at 1.3 mm.

Although both the CO(1–0) and CO(2–1) line profiles are complex, we could not justify the use of a more complex model than a simple Gaussian profile due to the poor S/N. To check the

validity of this approach, we also estimated the integrated flux by summing the spectra between $\pm 500 \,\mathrm{km\,s^{-1}}$; for both the CO(1–0) and (2–1) lines, this method produced values within the 1σ errors of the fluxes from the Gaussian fit.

To estimate the molecular gas mass from the integrated CO(1–0) line flux I_{CO}, we first estimated the total CO line luminosity L'_{CO} using equation (3) of Solomon et al. (1997)

$$L'_{\mathrm{CO}} = 3.25 \times 10^7 I_{\mathrm{CO}} \, [\nu_0 (1+z)]^{-2} \, D_{\mathrm{L}}^2 (1+z)^{-3}, \qquad (9)$$

where L'_{CO} has units $\mathrm{K\,km\,s^{-1}\,pc^2}$, the luminosity distance D_{L} is given in Mpc, the rest-frame emission line frequency ν_0 is given in GHz, and I_{CO} is given in $\mathrm{Jy\,km\,s^{-1}}$. As is standard for nearby ETGs, we used a Milky Way conversion factor between CO luminosity and H_2 gas mass, corresponding to $\alpha_{\mathrm{CO}} = 4.6 \,\mathrm{M_\odot} \, / \, [\mathrm{K\,km\,s^{-1}\,pc^2}]$, which gives a molecular gas mass $M_{\mathrm{H_2, CO}} = 1.1 \pm 0.4 \times 10^9 \,\mathrm{M_\odot}$.

5.3.1 Surface density of dense gas

Resolved CO observations suggest that CO emission traces dust in ETGs (Alatalo et al. 2013). Hence, because our CO observations are not spatially resolved, we estimated the dense gas mass surface density Σ_{gas} using the extinction as a proxy for the distribution of dense gas. At the frequency of the observed CO(1–0) transition, the FWHM of the IRAM beam is FWHM = $(2460/\nu_{\mathrm{obs}}[\mathrm{GHz}])$ arcsec = 21.9 arcsec, slightly smaller than the size of the ionized gas disc. As shown in Fig. 10, the IRAM beam covers roughly the same area over which we are able to measure A_V; over this region, A_V varies from 0 to 2 mag and has a clumpy distribution, showing no clear trends with radius. Hence it is reasonable for us to assume that the CO emission is uniformly distributed across the IRAM beam, which gives $\Sigma_{\mathrm{gas}} = 15 \pm 5 \,\mathrm{M_\odot\,pc^{-2}}$, consistent with our A_V-based estimate ($\Sigma_{\mathrm{gas}} = 10.0 \pm 0.5 \,\mathrm{M_\odot\,pc^{-2}}$.). We use this gas mass surface density estimate in Section 6.3 to investigate whether the jets are inducing negative feedback in UGC 05771.

6 DISCUSSION

In this section, we present our interpretation of our OSIRIS, CALIFA, and IRAM results. First, we argue that the shocked near-IR and optical line emission is due to jet–ISM interactions, and therefore that the radio source is much more extended than its apparent size in existing VLBI observations. We then use our CO observations and SFR estimates to determine whether the extended jet plasma is inhibiting star formation in UGC 05771. Finally, we constrain the properties of the density distribution of the ISM in UGC 05771 and estimate the age of the radio source.

6.1 Evidence for jet–ISM interaction in UGC 05771

Using our OSIRIS data (Section 3), we detected shocked molecular and ionized gas at radii of ≈ 200 pc, whereas the CALIFA data (Section 4) revealed shocked ionized gas at radii of ≈ 1 kpc. Here, we argue that both the optical and near-IR line emission is caused by the radio jets.

In Section 3.4.2, we showed that SNe explosions are unable to reproduce the observed [Fe II] line luminosity. Meanwhile, the [Fe II], H_2, and $H\alpha$ luminosities represent a few per cent of the estimated jet power ($4.2 \times 10^{41} \,\mathrm{erg\,s^{-1}}$), meaning it is energetically plausible for the jets to power the line emission via radiative shocks. The [Fe II] exhibits a sharp velocity gradient of $\approx 200 \,\mathrm{km\,s^{-1}}$ and has broad-line widths of up to $230 \,\mathrm{km\,s^{-1}}$ (Fig. 6), indicating this gas is

Table 3. Observational results for CO: Rest-frame and observed frequency, velocity offset to $z = 0.02469$, FWHM line width, peak brightness temperature, and integrated line flux.

Line	ν_0 (GHz)	ν_{obs} (GHz)	Δv (km s^{-1})	FWHM (km s^{-1})	T_{pk} (mK)	Flux I_{CO} (Jy km s^{-1})
CO(1–0)	115.271	112.4755 ± 0.0013	-49.4 ± 4.7	476 ± 23	2.9 ± 0.1	8.6 ± 0.4
CO(2–1)	230.538	224.9662 ± 0.0009	22.4 ± 11.5	562 ± 26	2.65 ± 0.1	11.9 ± 0.5

being excited by an energetic process. The radial velocities expected due to galactic rotation at these radii are insufficient to explain the velocity gradient in the [Fe II]. Meanwhile, there is no coherent rotation in the warm H_2, with most of the line emission being blueshifted (Fig. 3), suggesting this material is being ejected from the nucleus. The radial velocities of both the [Fe II] and the H_2 are too small for the gas to escape the host galaxy's potential, with $v_{esc} \approx 900$ km s^{-1} at comparable radii. We therefore conclude that both the H_2 and the [Fe II] emission probe gas being accelerated out of the nucleus by the jets, entrained in a 'stalling wind' that will not escape the host galaxy. Similar phenomena have previously been observed in NGC 1266 (e.g. Alatalo et al. 2015) and in 3C 326 N (Nesvadba et al. 2010, 2011), in which only a fraction of the emission line molecular gas accelerated by the jets exceeds the escape velocity of the host galaxy.

In our CALIFA data we detected a kpc-scale region of shocked gas with an elevated velocity dispersion in the vicinity of the nucleus. We have shown that beam smearing is unable to reproduce the observed velocity dispersion (Section 4.3), and that the line ratios in this region are consistent with shocks (Fig. 11b). We also demonstrated that it is highly unlikely that UGC 05771 is accreting enough material to drive these shocks, given the relatively ordered kinematics in the ionized gas disc, and the lack of any signatures of infalling gas (Section 4.3.4). Hence, we conclude that kpc-scale jet plasma must be responsible for this line emission.

However, the apparent size of the radio source is 9 pc (e.g. Fig. A1a). This is inconsistent with our hypotheses that the jets power the H_2 and [Fe II] emission, which extend $\approx$200 pc from the nucleus, and the H α emission, which extends $\approx$1 kpc from the nucleus. We address this in the following section.

6.2 How extended is the radio source?

The turnover frequency of GPS and CSS sources is strongly anticorrelated with the radio size of the source (O'Dea & Baum 1997). In Fig. 14, we show this correlation for the sample of GPS and CSS sources compiled by Jeyakumar (2016). We also indicate UGC 05771 on the plot (red star), using the linear size from the VLBI observations (de Vries et al. 2009; Fig. A1a and b). UGC 05771 is offset from the correlation by nearly two orders of magnitude, indicating it is possible that the radio source is in fact $\gtrsim$100 times more extended than its size in existing VLBI observations.

If the jets are oriented at a small angle θ to the LOS, the source will appear much more compact than it truly is. Such beamed sources generally exhibit high-flux variability. However, Snellen et al. (2004) find that UGC 05771 does not have significant flux variability at 5 and 8.4 GHz. We therefore conclude that the compactness of the radio source is not an orientation effect. Why, then, does it appear to be so small?

The linear size of the radio source associated with UGC 05771 is based on the VLBI observations of de Vries et al. (2009) at 1.665 GHz. Referring to Fig. 1, these VLBI observations recover
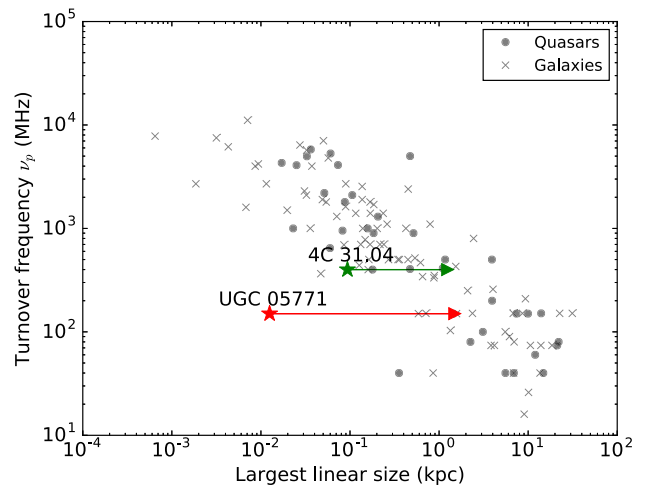

Figure 14. The peak frequency versus largest linear size for the catalogue of GPS and CSS sources compiled by Jeyakumar (2016), illustrating the strong anticorrelation between turnover frequency and linear size. The stars indicate the linear sizes, derived from VLBI observations, of 4C 31.04 (Zovaro et al. 2019, green) and UGC 05771 (red) presented by Giroletti et al. (2003) and de Vries et al. (2009), respectively. Meanwhile, the arrows indicate the approximate extent of ro-vibrational H_2 emission in in 4C 31.04 and optical emission line gas with line ratios consistent with shocks (Fig. 11b), which may trace extended, low surface brightness jet plasma that is resolved out in the VLBI images.

only 20–30 per cent of the unresolved single-dish fluxes at comparable frequencies. This implies that 70–80 per cent of the radio emission at these frequencies is emitted on scales larger than the spatial cut-off frequency of the VLBI observations.

The presence of bright, compact radio structures embedded in extended regions of low surface brightness radio emission is a key signature of jets in the 'flood-and-channel phase' of evolution (Sutherland & Bicknell 2007). In this phase, emergent jets split into multiple streams as they interact with a clumpy medium. Whilst the weaker streams percolate isotropically and form a bubble that drives a shock into the surrounding medium, the main jet stream emits brightly in the radio as it interacts with the ISM impeding its passage. Synthetic radio surface brightness images of these simulations (e.g. fig. 9 of Zovaro et al. 2019) show that the bubble can expand rapidly, enabling low surface brightness plasma to be much more extended than the brightest radio structures. The low-flux completeness of the pc-scale VLBI observations, coupled with the kpc-scale shocked gas, therefore suggests the jets in UGC 05771 are in the 'flood-and-channel phase', which we have previously observed in the CSS source 4C 31.04 (Zovaro et al. 2019). The possible presence of a counter-rotating core (Fig. 12c) may additionally be a signature of jets interacting with a clumpy disc (Mukherjee et al. 2018b), a phenomenon also observed in IC 5063 (Morganti et al. 2015; Mukherjee et al. 2018a).
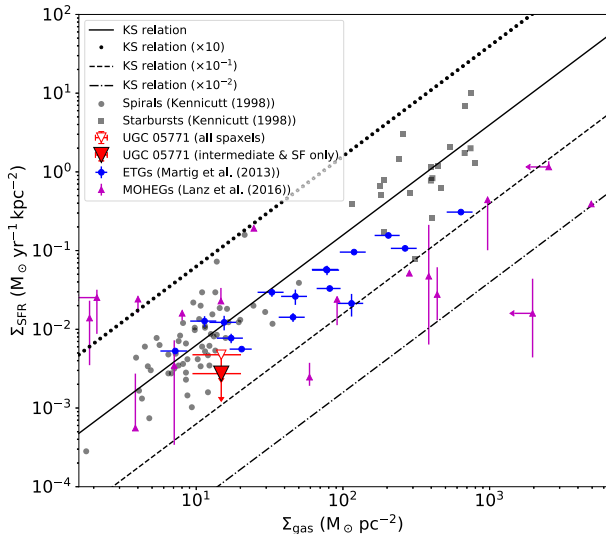
Figure 15. The Kennicutt–Schmidt (KS) relation. The black line represents the KS relation for a Salpeter IMF. We also show lines which display star forming efficiencies of $10\times$ (dotted line), $0.1\times$ (dashed line), and $0.01\times$ (dot–dashed line) that of the KS relation. We indicate UGC 05771 with 1σ error bars for Σ_{gas} and Σ_{SFR}, where we have adopted the H α-based SFR surface density computed using all spaxels within the IRAM beam (empty red triangle) and computed using only those spaxels with line ratios that lie in the intermediate or star-forming regions of the ODD shown in Fig. 11 (filled red triangle). The blue points are the sample of quiescent ETGs of Martig et al. (2013), where the SFRs have been estimated using the 8 μm flux, and the magenta points are the sample of radio galaxies of Lanz et al. (2016). The grey circles and squares are the sample of spiral and starburst galaxies of Kennicutt (1998). The SFRs for all samples have been adjusted for a Salpeter IMF.

6.3 Are the jets inducing negative feedback in UGC 05771?

Even if the jets in UGC 05771 are not powerful enough to prevent star formation by ejecting gas from the host galaxy's potential, our optical and near-IR observations indicate that there is kpc-scale jet plasma driving shocks and turbulence into the ISM. In this section, we use the Kennicutt–Schmidt (KS) relation (Kennicutt 1998) to determine whether the galaxy has a noticeable offset from that relation that could be attributed to the interactions with the radio jet.

Fig. 15 shows where UGC 05771 lies with respect to the KS relation (assuming a Salpeter IMF). To estimate Σ_{gas} in UGC 05771, we use our CO observations; for the SFR surface density Σ_{SFR}, we show our estimates computed using both the total H α flux (empty red triangle) and the H α flux only from spaxels with emission line ratios lying in the intermediate and star-forming regions of the optical diagnostic diagrams (filled red triangle). We favour the latter value, as the first is contaminated by gas where shocks, AGN photoionization, and/or photoionization from post-AGB stars dominates, as indicated by the line ratios.

For comparison, we also show galaxies from two different samples: 15 ETGs from Martig et al. (2013), which do not host AGNs, but may show signatures of morphological quenching, and 16 bright, gas-rich radio galaxies ('molecular hydrogen emission galaxies', MOHEGs) from Lanz et al. (2016), which contain warm, shocked molecular gas, presumably from interactions with the radio jet (Nesvadba et al. 2010; Ogle et al. 2010). The SFRs in these samples were derived from PAHs and the far-IR dust emission,

respectively, which may imply small systematic uncertainties of order 0.1–0.2 dex compared to UGC 05771.

We also show the original sample of spiral and starburst galaxies from Kennicutt (1998), where the SFRs have been estimated using H α and FIR fluxes respectively, both adjusted for a Salpeter IMF. Adopting the SFR(H α) estimate only using the intermediate and star-forming spaxels, UGC 05771 is shifted by a factor of 9 from the KS relationship of ordinary star-forming galaxies, corresponding to a shift of about 1σ, and in the regime covered by the samples of Martig et al. (2013) and Lanz et al. (2016). However, as discussed in Section 4.3.3, our Σ_{SFR} estimate should be interpreted as an upper limit due to contamination from shocks, AGN photoionization, and/or post-AGB stars. It is therefore feasible that UGC 05771 is even more strongly offset. Spatially resolved observations would be needed to see whether this offset of the global, source averaged gas and star formation surface densities heralds a more pronounced, local decrease in star formation efficiency, or whether a slight global decrease is happening in UGC 05771. This would also help to distinguish whether such a decrease would be due to interactions with the radio jet, or other quenching mechanisms, e.g. morphological quenching. Regardless of the detailed mechanism in place, however, our results do show that UGC 05771 has a slightly lower SFR than would be expected from the KS law at face value.

6.4 Constraining the parameters of the ISM density distribution

Free–free absorption (FFA) of synchrotron radiation by an inhomogeneous ionized medium enshrouding the jet plasma can replicate the characteristic spectrum of GPS and CSS sources (Bicknell et al. 2018). Under this paradigm, the frequency of the spectral peak is sensitive to the density probability distribution function (PDF) of the ISM. Here, we use the method of Zovaro et al. (2019) to infer the properties of the density PDF in UGC 05771; for full details of the method, we refer the reader to their section 5.4.

We modelled the ISM as having a lognormal density distribution, which is appropriate for turbulent media (Nordlund & Padoan 1999; Federrath & Klessen 2012), and assumed the absorbing medium is a slab with depth $L = 2$ kpc, corresponding to the region of elevated velocity dispersion in the ionized gas (Fig. 9d). Equation (17) of Zovaro et al. (2019) gives the free–free optical depth τ_ν as a function of ISM parameters shown in Table 4 and the expected value of n^2 in the slab $E(n^2)$. We estimated $E(n^2)$ by setting $\tau_\nu = 1$ at the spectral peak ν_p, and used equations (11)– (13) and (18) of Zovaro et al. (2019) to estimate the mean density $\bar{n}$ and the standard deviation σ of the density PDF, shown in Table 4. The low mean density ($\sim 1\,\mathrm{cm}^{-3}$) is consistent with the low-frequency spectral turnover of UGC 05771, whereas the inferred high turbulent Mach number and the assumption of a lognormal distribution gives a large value for $E(n^2)$.

We then estimated the age of the radio source using the extent of the shocked gas, our new density estimate, and the jet power. Assuming that the jet-driven bubble evolves adiabatically, the time taken t_b for the bubble to reach its current size R_b if inflated by a jet with power L_{jet} expanding into a uniform medium with density ρ is given by (Bicknell & Begelman 1996)

$$t_b = \left(\frac{384\pi}{125}\right)^{1/3} \rho^{1/3} L_{jet}^{-1/3} R_b^{5/3}, \tag{10}$$

where we adopted $R_b = 2$ kpc and a density $n = 1\,\mathrm{cm}^{-3}$ consistent with our FFA model. This gives an age of approximately 19 Myr.

Table 4. Parameters used in determining the parameters of the lognormal density distribution. Output parameters are denoted with daggers (†). Fractional abundances were estimated using a MAPPINGS V (Sutherland et al. 2013) model grid with non-equilibrium cooling and solar abundances.

Parameter	Symbol	Value
Peak frequency	ν_p	150 MHz
Depth of absorbing slab	L	2 kpc
Temperature	T	10^4 K
Mean molecular mass	μ	0.66504
Electron fractional abundance	n_e/n	0.47175
H^+ fractional abundance	n_{H^+}/n	0.41932
He^+ fractional abundance	n_{He^+}/n	0.024458
He^{++} fractional abundance	$n_{He^{++}}/n$	0.013770
Line-of-sight velocity dispersion	σ_g	225 km s^{-1}
Sound speed	c_s	11.21 km s^{-1}
Turbulent Mach number	$\mathcal{M}$	34.75 km s^{-1}
Turbulent forcing parameter	b	0.4
Ratio of thermal to magnetic pressure	β	1 (equipartition)
Expected value of n^2 †	$E(n^2)$	116.7 cm^{-6}
Mean density†	$\bar{n}$	1.094 cm^{-3}
Density variance†	σ^2	115.5 cm^{-6}

7 CONCLUSION

We have studied jet–ISM interactions in the low-power CSS source UGC 05771 in order to search for evidence that the jets are inhibiting star formation in the host galaxy.

We analysed the sub-kpc scale circumnuclear gas of the host galaxy to search for signatures of jet–ISM interactions using near-IR integral field spectroscopy from OSIRIS.

We detected ro-vibrational H_2 emission in the central 200 pc of the host galaxy that probes shock-heated molecular gas at $T \approx 5000$ K. We also detected [Fe II]$_{1.644\,\mu m}$ emission in the same region with luminosity too high to be explained by SNe explosions, whereas the jet power is sufficient to power both the [Fe II] and H_2 luminosities, leaving shocks induced by the jets as the most likely cause. The kinematics of both the H_2 and [Fe II] emission lines imply that the jets are accelerating material out of the nucleus to velocities insufficient to expel the gas from the host galaxy potential, creating a 'stalling wind'.

We analysed the properties of the kpc-scale optical emission line gas in the galaxy using optical integral field spectroscopy from the CALIFA survey. The host galaxy has a disc of ionized gas approximately 20 kpc in diameter. Line ratios, broad-line widths, and disturbed kinematics in the innermost 2 kpc cannot be explained by beam smearing or by accretion, indicating that the gas in this region is being shocked and disturbed by the jets. Further observations with higher spectral resolution are required to confirm the presence of multiple kinematic components in the emission lines that would arise from jet–ISM interactions.

Both the CALIFA and OSIRIS data show that the jets are interacting strongly with the ISM out to kpc radii, in apparent contradiction to the pc-scale structure revealed by VLBI imaging. We proposed that UGC 05771 in fact hosts a kpc-scale radio source, and that the extended jet plasma is either resolved out by these observations or has too low a surface brightness to be detected, consistent with the location of UGC 05771 on the peak frequency–size correlation.

To determine whether the jets are inhibiting star formation in UGC 05771, we obtained IRAM observations of CO(1–0) and CO(2–1), and found $M_{gas} = 1.1 \pm 0.4 \times 10^9$ M$_\odot$ and a mean sur-

face density $\Sigma_{gas} = 15 \pm 5$ M$_\odot$ pc^{-2}. Although we found that it is possible that UGC 05771 is significantly offset from the KS relation, we were unable to confirm whether negative feedback is taking place due to systematic uncertainties in our H α-based SFR estimate due to contamination by shocks and evolved stars.

The fact that we have observed signatures of jet–ISM interactions out to kpc radii in both 4C 31.04 and UGC 05771 suggests that diffuse, low surface brightness radio plasma that is not visible in VLBI observations may be common in compact radio galaxies. Our observations have shown that this radio plasma interacts strongly with the ISM, heating and injecting turbulence, and potentially inhibiting star formation. This finding demonstrates that young radio sources with seemingly compact jets may have a substantial impact on the star formation of their host galaxy, having important implications for the role that jets play in galaxy evolution.

---

[5] Available https://www.mpe.mpg.de/ ott/QFitsView/.
[6] Available http://www.scipy.org/.

et al. 2001), and ASTROPY,[7] a community-developed core PYTHON package for Astronomy (Astropy Collaboration 2013, 2018).

REFERENCES

Alatalo K. et al., 2013, MNRAS, 432, 1796
Alatalo K. et al., 2015, ApJ, 798, 31
Astropy Collaboration, 2013, A&A, 558, A33
Astropy Collaboration, 2018, AJ, 156, 123
Baldwin J. A., Phillips M. M., Terlevich R., 1981, PASP, 93, 5
Belfiore F. et al., 2016, MNRAS, 461, 3111
Bender R., 1988, A&A, 202, L5
Bicknell G. V., Begelman M. C., 1996, ApJ, 467, 597
Bicknell G. V., Mukherjee D., Wagner A. Y., Sutherland R. S., Nesvadba N. P. H., 2018, MNRAS, 475, 3493
Calzetti D., 2013, in Falcón-Barroso J., Knapen J., eds, Star Formation Rate Indicators, Cambridge Univ. Press. Cambrige, p. 419
Cheng X.-P., An T., 2018, ApJ, 863, 155
Croton D. J. et al., 2006, MNRAS, 365, 11
Dabrowski I., 1984, Can. J. Phys., 62, 1639
Davies R. I., 2007, MNRAS, 375, 1099
de Vries N., Snellen I. A. G., Schilizzi R. T., Mack K.-H., Kaiser C. R., 2009, A&A, 498, 641
Fabian A. C., 2012, ARA&A, 50, 455
Falco E. E. et al., 1999, PASP, 111, 438
Federrath C., Klessen R. S., 2012, ApJ, 761, 156
Fitzpatrick E. L., Massa D., 2007, ApJ, 663, 320
Fomalont E. B., Kellermann K. I., Partridge R. B., Windhorst R. A., Richards E. A., 2002, AJ, 123, 2402
Gildas Team, 2013, Astrophysics Source Code Library, record ascl:1305.010
Giroletti M., Giovannini G., Taylor G. B., Conway J. E., Lara L., Venturi T., 2003, A&A, 399, 889
Guillard P., Boulanger F., Lehnert M. D., Pineau des Forêts G., Combes F., Falgarone E., Bernard-Salas J., 2015, A&A, 574, A32
Gültekin K. et al., 2009, ApJ, 698, 198
Güver T., Özel F., 2009, MNRAS, 400, 2050
Holt J., Tadhunter C. N., Morganti R., 2008, MNRAS, 387, 639
Ineson J., Croston J. H., Hardcastle M. J., Mingo B., 2017, MNRAS, 467, 1586
Jeyakumar S., 2016, MNRAS, 458, 3786
Jones E. et al., 2001, SciPy: Open source scientific tools for Python. Available at: http://www.scipy.org/
Kauffmann G. et al., 2003, MNRAS, 346, 1055
Kennicutt R. C., Jr, 1998, ApJ, 498, 541
Kewley L. J., Dopita M. A., Sutherland R. S., Heisler C. A., Trevena J., 2001, ApJ, 556, 121
Kewley L. J., Groves B., Kauffmann G., Heckman T., 2006, MNRAS, 372, 961
Lanz L., Ogle P. M., Alatalo K., Appleton P. N., 2016, ApJ, 826, 29
Larkin J. et al., 2006, in McLean I. S., Iye M., eds, Proc. SPIE Conf. Ser. Vol. 6269, Ground-based and Airborne Instrumentation for Astronomy. SPIE, Bellingham, p. 62691A
Leitherer C. et al., 1999, ApJS, 123, 3
Markwardt C. B., 2009, in Bohlender D. A., Durand D., Dowler P., eds, ASP Conf. Ser. Vol. 411, Astronomical Data Analysis Software and Systems XVIII. Astron. Soc. Pac., San Francisco, p. 251
Martig M. et al., 2013, MNRAS, 432, 1914
McNamara B. R., Nulsen P. E. J., 2012, New J. Phys., 14, 055023
Merloni A., Heinz S., di Matteo T., 2003, MNRAS, 345, 1057
Moré J. J., 1978, The Levenberg-Marquardt Algorithm: Implementation and Theory. Springer, Berlin, Heidelberg, p. 105
Morganti R., Fogasy J., Paragi Z., Oosterloo T., Orienti M., 2013, Science, 341, 1082

Morganti R., Oosterloo T., Oonk J. B. R., Frieswijk W., Tadhunter C., 2015, A&A, 580, A1
Mukherjee D., Bicknell G. V., Sutherland R., Wagner A., 2016, MNRAS, 461, 967
Mukherjee D., Wagner A. Y., Bicknell G. V., Morganti R., Oosterloo T., Nesvadba N., Sutherland R. S., 2018a, MNRAS, 476, 80
Mukherjee D., Bicknell G. V., Wagner A. Y., Sutherland R. S., Silk J., 2018b, MNRAS, 479, 5544
Murgia M., 2003, Publ. Astron. Soc. Aust., 20, 19
Nesvadba N. P. H., Lehnert M. D., Eisenhauer F., Gilbert A., Tecza M., Abuter R., 2006, ApJ, 650, 693
Nesvadba N. P. H. et al., 2010, A&A, 521, A65
Nesvadba N. P. H., Boulanger F., Lehnert M. D., Guillard P., Salome P., 2011, A&A, 536, L5
Neugebauer G. et al., 1984, ApJ, 278, L1
Nordlund Å. K., Padoan P., 1999, in Franco J., Carramina A., eds, Interstellar Turbulence, Proceedings of the 2nd Guillermo Haro Conference, The Density PDFs of Supersonic Random Flows, Cambridge Univ. Press, Cambridge, p. 218
Ocaña Flaquer B., Leon S., Combes F., Lim J., 2010, A&A, 518, A9
O'Dea C. P., 1998, PASP, 110, 493
O'Dea C. P., 2016, Astron. Nachr., 337, 141
O'Dea C. P., Baum S. A., 1997, AJ, 113, 148
Ogle P., Boulanger F., Guillard P., Evans D. A., Antonucci R., Appleton P. N., Nesvadba N., Leipski C., 2010, ApJ, 724, 1193
Oh K., Sarzi M., Schawinski K., Yi S. K., 2011, ApJS, 195, 13
Orienti M., 2016, Astron. Nachr., 337, 9
Puxley P. J., Hawarden T. G., Mountain C. M., 1990, ApJ, 364, 77
Rosenberg M. J. F., van der Werf P. P., Israel F. P., 2012, A&A, 540, A116
Rosenberg M. J. F., van der Werf P. P., Israel F. P., 2013, A&A, 550, A12
Roth M. M. et al., 2005, PASP, 117, 620
Rowan-Robinson M. et al., 1997, MNRAS, 289, 490
Salim S. et al., 2007, ApJS, 173, 267
Sánchez S. F. et al., 2012, A&A, 538, A8
Sánchez S. F. et al., 2016, Rev. Mex. Astron. Astrofis., 52, 171
Saulder C., van Kampen E., Chilingarian I. V., Mieske S., Zeilinger W. W., 2016, A&A, 596, A14
Silk J., Rees M. J., 1998, A&A, 331, L1
Singh R. et al., 2013, A&A, 558, A43
Snellen I. A. G., Mack K.-H., Schilizzi R. T., Tschager W., 2004, MNRAS, 348, 227
Solomon P. M., Downes D., Radford S. J. E., Barrett J. W., 1997, ApJ, 478, 144
Sutherland R. S., Bicknell G. V., 2007, ApJS, 173, 37
Sutherland R., Dopita M., Binette L., Groves B., 2013, Astrophysics Source Code Library, record ascl:1306.008
Tadhunter C., Morganti R., Rose M., Oonk J. B. R., Oosterloo T., 2014, Nature, 511, 440
Terzić B., Graham A. W., 2005, MNRAS, 362, 197
Turner J., Kirby-Docken K., Dalgarno A., 1977, ApJS, 35, 281
van Dam M. A. et al., 2006, PASP, 118, 310
Veilleux S., Osterbrock D. E., 1987, ApJS, 63, 295
Wagner A. Y., Bicknell G. V., Umemura M., Sutherland R. S., Silk J., 2016, Astron. Nachr., 337, 167
Walcher C. J. et al., 2014, A&A, 569, A1
Willett K. W., Stocke J. T., Darling J., Perlman E. S., 2010, ApJ, 713, 1393
Wizinowich P. L. et al., 2006, PASP, 118, 297
Wolniewicz L., Simbotin I., Dalgarno A., 1998, ApJS, 115, 293
Zovaro H. R. M., Sharp R., Nesvadba N. P. H., Bicknell G. V., Mukherjee D., Wagner A. Y., Groves B., Krishna S., 2019, MNRAS, 484, 3393

APPENDIX A: THE MORPHOLOGY OF THE RADIO SOURCE

The radio source associated with UGC 05771 has a strikingly different morphology at 1.665 GHz (Fig. A1a), 4.993 GHz (Fig. A1b), and at 8.4 GHz (Fig. A1c). A south-west (SW) component at a

---

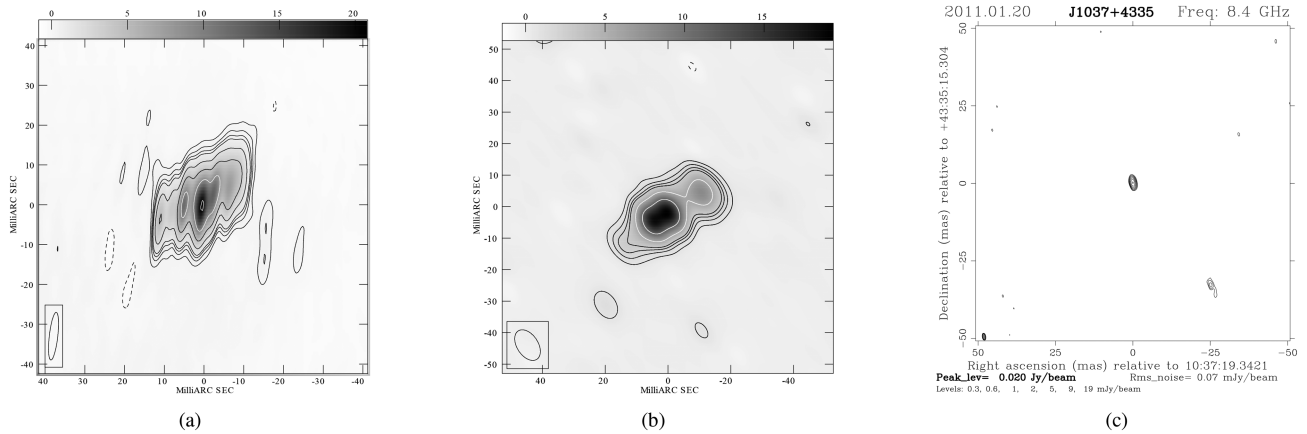[7] Available http://www.astropy.org.

Figure A1. (a) and (b) show VLBI images of UGC 05771 at 1.665 GHz and 4.993 GHz, respectively (de Vries et al. 2009, A&A, 498, 641, 2009, reproduced with permission © ESO). (c) shows the VLBI image at 8.4 GHz, obtained from the astrogeo data base.[8] The root-mean-square (rms) sensitivities for these observations are 0.10, 0.23, and 0.09 mJy beam^{-1}, respectively.

projected distance of 18.3 pc is visible at 8.4 GHz; whilst there is faint contour to the SW at 4.993 GHz, it is absent at 1.665 GHz. In this section we address the apparent discrepancies between the three images.

The SW contour is offset by ≈16 mas (7.1 pc) between the 4.993 and 8.4 GHz images. The observations are separated by 6.6 yr, corresponding to an apparent speed of ≈3.5c, which would only be plausible if the source were strongly beamed. We rule this out due to the source's low-flux variability (Snellen et al. 2004); therefore the SW contour in the 4.993 GHz image is probably an artefact.

Using the 8.4 GHz radio source count of Fomalont et al. (2002) we estimate the likelihood that the SW component is a background source to be vanishingly small, and therefore is most probably associated with UGC 05771. It is instead likely to be a site where jet plasma has interacted with a particularly dense cloud in the ISM, re-accelerating electrons and creating a temporary hotspot.

The SW component may be absent from the 1.665 and 4.993 GHz images due to beam smearing. If the integrated flux of a point source is lower than the rms noise per beam, the component will be indistinguishable from noise. The integrated flux of the SW component at 8.4 GHz is $S_{int}(8.4\,Ghz) = 2.13$ mJy (Cheng & An

2018). Assuming the spectral index of the source $\alpha = 0.62$ (Snellen et al. 2004), then the integrated fluxes $S_{int}(5.0\,Ghz) = 2.94$ mJy and $S_{int}(1.7\,Ghz) = 5.74$ mJy. The rms noise of the observations is 0.23 and 0.10 mJy beam^{-1} at 4.993 and 1.665 GHz, respectively, meaning that the SW component would be detected with a high S/N in either case; hence beam smearing cannot explain why the component is not visible.

We conclude that either (i) the SW component is strongly absorbed at these frequencies, either by synchrotron self-absorption or FFA, or (ii), there is structure at these lower frequencies that has been resolved out, which is consistent with the low-flux completeness of these observations (≤ 30 per cent, see Fig. 1). For example, the jet structure visible at 1.7 and 5 GHz is absent at 8.4 GHz. Using the flux along the jet axis from Fig. A1(b) and assuming $\alpha = 0.62$, the emission at 8.4 GHz should be ≈5 mJy, well above the rms noise (0.07 mJy), indicating that the jets have been resolved out in these observations. It is therefore plausible that the SW component has lower frequency counterparts that are not visible in these observations.

This paper has been typeset from a TEX/LATEX file prepared by the author.